Remote Sensing of Environment 341 (2026) 115456

Contents lists available at ScienceDirect

Remote Sensing of Environment

journal homepage: www.elsevier.com/locate/rse

Tracing changes in subsurface water storage through a novel satellite-based time-series of far-red solar-induced fluorescence quantum efficiency

David Herrera [a,*], Alexandre Belleflamme [b], Klaus Görgen [b], Uwe Rascher [a,c], Bastian Siegmann [a,d]

[a] Forschungszentrum Jülich GmbH, Institute of Bio- and Geosciences, IBG-2: Plant Sciences, Leo-Brandt-Str., 52425 Jülich, Germany
[b] Forschungszentrum Jülich GmbH, Institute of Bio- and Geosciences, IBG-3: Agrosphere, Leo-Brandt-Str., 52425 Jülich, Germany
[c] University of Bonn, Faculty of Agricultural, Nutritional and Engineering Sciences, Institute of Crop Science and Resource Conservation, Karlrobert-Kreiten-Strasse 13, 53115 Bonn, Germany
[d] Faculty of Geo-Information Science and Earth Observation (ITC), University of Twente, P.O. Box 217, Enschede 7500 AE, the Netherlands

ARTICLE INFO

Edited by Jing M. Chen

Keywords:
SIF
Drought stress
TROPOMI
MODIS
Normalization
Downscaling

ABSTRACT

Passive optical satellite products have long been used to trace drought effects. Effective mitigation and understanding land–atmosphere interactions require variables reflecting plant physiological status under water scarcity. One such variable is Solar-Induced Chlorophyll Fluorescence (SIF), emitted directly from the photosynthetic apparatus. It provides direct information on vegetation functioning and can reveal stress within days. Spaceborne SIF observations have been available for over a decade and have been widely applied for vegetation stress detection. However, robust daily drought monitoring remains challenging because top-of-canopy SIF is strongly modulated by canopy structure and illumination, and retrieval noise can obscure short-term drought responses. This motivates normalization approaches that better isolate the physiological component of the fluorescence signal for near-real-time drought monitoring. To address this limitation, we estimated leaf-level fluorescence quantum efficiency (ΦF) by integrating TROPOMI SIF with photosynthetically active radiation (PAR) from the Breathing Earth Simulator (BESS), generating a daily 0.05° dataset for Germany (2018–2023). We evaluated ΦF as an early drought indicator in agricultural and forest ecosystems by comparing it with a subsurface water storage anomaly (SSWS) product from the coupled ParFlow/CLM model. Drought periods were identified as prolonged negative SSWS anomalies. Daily ΦF was aggregated, smoothed with a two-day rolling average, and analyzed via lagged cross-correlation with surrogate-based significance testing. ΦF consistently tracked negative SSWS anomalies with a two-day lag. This pattern was consistent across across the two analyzed land-cover classes, indicating that ΦF detects emerging reductions in subsurface water storage with a short delay. MODIS land surface temperature (LST) exhibited a complementary inverse response, peaking at 1–2 days underscoring that the correlation found was in fact linked to water availability. In contrast, TOC SIF and common vegetation indices (NIRv, NDVI) showed weak or inconsistent correlations. These results demonstrate that ΦF enables near-real-time detection of vegetation water stress and outperforms traditional optical indices for this purpose. The study highlights the need for downscaling and normalization to transform canopy SIF observations into an effective signal for early drought detection.

1. Introduction

Europe has been experiencing an increasing number of drought events over the past decade. The 2018–2020 drought is considered to be a new benchmark and is a glimpse into future extreme events exacerbated by global climate change (Rakovec et al., 2022). Especially the increasing number of consecutive droughts are a danger for forestry and agriculture, not only in southern but also in central and northern Europe as depleted subsurface water resources are not able to recover (Hari et al., 2020; Belleflamme et al., 2023). Drought impacts are commonly categorized based on their primary driver and their propagation through the land surface. Meteorological droughts are defined as precipitation

* Corresponding author.
E-mail addresses: d.herrera@fz-juelich.de (D. Herrera), a.belleflamme@fz-juelich.de (A. Belleflamme), k.goergen@fz-juelich.de (K. Görgen), u.rascher@fz-juelich.de (U. Rascher), b.siegmann@fz-juelich.de (B. Siegmann).

https://doi.org/10.1016/j.rse.2026.115456
Received 20 September 2025; Received in revised form 23 April 2026; Accepted 25 April 2026
Available online 30 April 2026

deficits that can lead to soil moisture deficits which in turn are defined as agricultural droughts. The effects can be detected in wilting of plants once the soil moisture drops below a certain threshold and affect agricultural yield and forest health (Boergens et al., 2020; West et al., 2019; Senf and Seidl, 2021).

These droughts can be tracked using a combination of soil moisture, precipitation and optical remote sensing data that reflect vegetation health. Such data are used in various drought monitors both on national and continental scale (Svoboda et al., 2002; Sepulcre-Canto et al., 2012; Carrão et al., 2016; Zink et al., 2016; Trnka et al., 2020; Cammalleri et al., 2021; Belleflamme et al., 2023). The European Drought Observatory (EDO) for instance uses the anomaly of the standardized precipitation index (SPI), and the soil moisture anomaly (derived from radar satellite data) in combination with anomaly of the fraction of absorbed photosynthetically active radiation (fAPAR) (derived from optical satellite data) to define drought risk in Europe at an interval of ten days (Fioravanti et al., 2025). The combination of the three components makes up the classification of drought risk of the Combined Drought Indicator (CDI). A negative SPI anomaly value indicates the onset of a drought event and consequently an observed area is classified as 'watch'. When additionally, the soil moisture anomaly is getting negative the area is classified as 'warning'. Lastly, when the vegetation component represented by the fAPAR anomaly also becomes negative the observed area is classified as 'alert' (Sepulcre-Canto et al., 2012).

The optical component therefore detects the reaction of vegetation to drought stress. This vegetation response component differs between various drought monitors. It can be defined as the vegetation health index (VHI) a combination of the NDVI and the brightness temperature (BT) used by the U.S. drought monitor or as a simple reflectance-based vegetation index such as the EVI2 that is used by the Czech drought monitor (Svoboda et al., 2002; Trnka et al., 2020). Such VI's are linked to the greenness of observed ecosystems and thus have the potential to track the reaction of vegetation to insufficient water supply within approximately a month depending on the ecosystem (Hua et al., 2019). Similarly, fAPAR, which represents the canopy's energy absorption capacity, has been proven suitable for detecting drought effects at the satellite scale within approximately 20 days (Fensholt et al., 2004; Quirós and Fragoso-Campón, 2024). At these temporal scales, however, fAPAR primarily reflects chlorophyll degradation and structural changes in the canopy, such as leaf wilting or altered leaf orientation, whereas the earliest physiological response to drought is stomatal closure, which, if the stress persists, leads to reduced photosynthetic rates (Berger et al., 2022).

Remotely-sensed solar-induced chlorophyll fluorescence (SIF) has the potential to be used as a more direct indicator of water deficiency of vegetation because it is emitted from the core of the photosynthetic apparatus (Drusch et al., 2017). SIF is a byproduct of photosynthesis and thus can be used to determine photosynthetic efficiency and functioning. When abiotic stress occurs due to an increased dissipation of thermal energy through the process of non-photochemical quenching (NPQ), the fluorescence yield decreases (Berger et al., 2022; Damm et al., 2018). The potential of SIF as a drought stress indicator and a potential candidate to support in drought monitoring has been shown by Geng et al. (2022) at monthly temporal resolution. A combination of existing drought detection schemes and SIF has been developed in recent years that could help in tracking drought on both the basis of meteorological data and the actual physiological state of plants (Zhang et al., 2021a; Liu et al., 2021, 2023a). These drought detection approaches using SIF have so far been developed based on 8-day or monthly satellite data. SIF, however, can potentially detect drought responses within only a few days (De Cannière et al., 2022). Monitoring these responses could help mitigate drought rather than simply determine its effects.

Since SIF only makes up between 1 and 5% of reflected radiance, its retrieval requires imaging spectrometers with subnanometer spectral resolution to detect infilling in specific atmospheric absorption features. To date, these requirements have only been met by satellite sensor systems designed for atmospheric applications, which allowed for the first retrieval of SIF in 2011 using the Greenhouse gases Observing SATellite (GOSAT) (Frankenberg et al., 2011; Joiner et al., 2011). As a result, current satellite SIF products are derived from sensors that enable fluorescence retrieval, but were not specifically designed for this purpose. In 2026 this will change with the launch of the Fluorescence Explorer (FLEX) mission by ESA (European Space Agency, 2025). FLEX is especially designed for retrieving SIF and high-level vegetation products at 300 m GSD with a 27-day revisiting cycle at the equator (Drusch et al., 2017). While this mission will vastly improve our understanding of the vegetation status from space, the early detection of first drought symptoms through SIF requires a much higher revisit frequency. Daily satellite SIF data are available from the Global Ozone Monitoring Experiment-2 (GOME-2) aboard MetOP and Sentinel-5P's TROPOspheric Monitoring Instrument (TROPOMI). TROPOMI data is available at a higher spatial resolution of 0.05° compared to GOME-2 with 0.5° while maintaining the same temporal resolution. For this reason, TROPOMI data is better suited for tracking short-term drought effects caused by insufficient water supply, since its spatial resolution still allows the distinction of different biomes. SIF products derived from TROPOMI offer top of canopy SIF data on a daily basis since 2018 (Guanter et al., 2021; Köhler et al., 2018a). Two of these products, namely the TROPOSIF (Guanter et al., 2021) and Caltech TROPOMI SIF product (Köhler et al., 2018b), demonstrate good consistency with each other and with other satellite SIF datasets and are ideal candidates for studying vegetation stress at ecosystem scale(Guanter et al., 2021; Köhler et al., 2018a).

Top of canopy SIF is influenced by canopy structure and illumination conditions. For this reason, the downscaling and normalization of SIF from canopy to leaf level and calculating the fluorescence quantum efficiency at leaf level (ΦF) are vital to detect physiological changes that are directly linked to the photosynthetic activity of plants (Dechant et al., 2020). The calculation requires information about the fluorescence escape probability (fesc), which describes the fraction of emitted SIF that escapes the canopy in sensor direction (Guanter et al., 2014), and fAPAR.

According to Zeng et al. (2019) the product of these two variables can be approximated using the near infrared reflectance of vegetation index (NIRv). NIRv can be calculated as the product of the NDVI and near-infrared reflectance (Badgley et al., 2017). It can then be used to calculate the NIRvP, which is the product of NIRv and PAR (Dechant et al., 2022). The NIRv concept was used in numerous studies to predict Gross Primary Productivity (GPP) from SIF satellite data (e.g., Zeng et al., 2019; Jiang et al., 2021; Liu et al., 2023b). In this regard, Liu et al. (2023a) used TROPOMI and MODIS data to create an 8-day ΦF product that is able to track seasonal GPP variations better than TOC TROPOMI SIF. Besides NIRv other approaches have been developed determining fesc to downscale SIF such as the FCVI (Yang et al., 2020) and NIRvH (Zeng et al., 2021), however, these are not applicable to TROPOMI data because they require hyperspectral reflectance information in the visible spectral range.

Although TROPOMI provides near-daily SIF observations, many applications have relied on temporally aggregated products or on broad-scale analyses of vegetation response (Li et al., 2023a). Recent work has demonstrated the potential of daily fluorescence-based indicators for studying rapid vegetation dynamics and drought response timing (Tang et al., 2026; Wen et al., 2025). However, the development and evaluation of a dedicated daily fluorescence quantum efficiency (ΦF) product for fine-resolution regional drought monitoring remains limited.

Building on the approach presented by Liu et al. (2023a), we generate a novel ΦF satellite dataset for Germany with daily temporal and 0.05° spatial resolution covering six vegetation periods from 2018 to 2023. To evaluate its suitability for drought monitoring, we compare the dataset against anomalies of subsurface water storage (SSWS), derived from the Common Land Model (CLM) coupled with the hydrological model ParFlow (Belleflamme et al., 2023). This provides a basis

for assessing whether daily ΦF can support the early detection of drought stress at ecosystem scale.

2. Material and methods

2.1. Study site

While SIF satellite data is available globally, the SSWS reference dataset to accurately determine if normalized SIF can be used for drought detection was available for Germany only. This study splits the available data over Germany into agricultural and forested areas (Fig. 1, A) and uses three satellite products to calculate ΦF (Fig. 1, B, C, D) (Table 1). 50% of land use in Germany is classified as agricultural areas, while forested areas make up 29,9% (Bundesministerium für Ernährung und Landwirtschaft, 2025).Because these classes are defined on a coarser analysis grid than the original land-cover product, Fig. 1, E shows the proportional land-cover composition within pixels assigned to the agricultural and forest masks and is included to provide context on the degree of subpixel mixing in both classes.Though there has been an increasing trend in recent years to use irrigation, nationwide 95% of agriculture is still non-irrigated (Bernhardt et al., 2026). This lack of irrigation makes Germany an ideal candidate to detect agricultural drought stress through satellite data.

2.2. Satellite data

The spaceborne data used in this study were recorded by the ESA satellite Sentinel-5 Precursor (S-5P) and the NASA satellite constellation Aqua and Terra which carry the Moderate resolution imaging spectroradiometer (MODIS). The satellite data cover the period May 2018 to October 2023 with daily temporal resolution. Both datasets were gridded to 0.05°. To decrease processing times, as many processing steps as possible were performed in Google Earth Engine (GEE) (Gorelick et al., 2017).

2.2.1. Sentinel-5P - TROPOSIF products

The single payload satellite S-5P carries the TROPOspheric Monitoring Instrument (TROPOMI). An imaging spectrometer that was designed to monitor trace gases and aerosols in the Earth's atmosphere (Veefkind et al., 2012). It was launched in October 2017 and has been delivering data since May 2018. The wide swath of 2600 km allows for near-daily global coverage at a maximum spatial resolution of 0.05° at 13:30 local solar time. Bands 5 and 6 of the instrument cover the two spectral regions that are relevant for the retrieval of SIF (665–785 nm). The overlap of orbits allows for multiple observations per bin. To keep the normalization methodology coherent and ensure the same overpass time for all pixels within an orbit only the observations were used that were within the main orbit. Therefore, no averaging was applied.

2.2.1.1. SIF740. The SIF product used in this study is the L2B SIF dataset (v.1.0.0) produced within the ESA TROPOSIF project (Guanter et al., 2021). SIF is retrieved from TROPOMI using a data driven approach within two spectral windows (735–758, 743–758 nm). The latter is described as being the more reliable product and shows similar results to the Caltech SIF product also retrieved from TROPOMI data by Köhler et al. (2018a) (Guanter et al., 2021). The TROPOSIF dataset also provides day-length-scaled SIF that accounts for measurement time, sunrise and sunset, and the cosine of the solar zenith angle, following an adapted approach from Frankenberg et al. (2011). This addition allows for the comparison to other SIF satellite products that were recorded at different overpass times (Guanter et al., 2021). This data was used in our study to have a representative value of SIF per day as it was used by Balde et al. (2023), Pickering et al. (2022) and Doughty et al. (2019). The dataset is available in the form of an ungridded L2B product, which was gridded to the highest possible resolution of 0.05° per time point. While the data are available at near-daily temporal resolution, with only a few days missing per vegetation period, data availability in Germany is strongly affected by cloud cover. On average, the percentage of valid observations per vegetation period and land cover class used in this study amounts to 32% for forest-classified pixels and 33% for pixels classified as agricultural. Temporal averaging was applied in the form of a 2-day moving average at the last step of the analysis (see Section 3.2).

2.2.1.2. NIRv. The TROPOSIF product also includes top of atmosphere reflectance bands in the red, far red and near infrared (NIR) region at 665, 680, 712, 741, 755, 773, and 781 nm, respectively. Identical to Guanter et al. (2021), the reflectance bands at 665 nm (Red) and 781 nm (NIR) were used for the calculation of the near-infrared reflectance of vegetation (NIRv) index (Badgley et al., 2017) (Eq. (1)).

$$NIRv = \frac{(NIR - Red)}{(NIR + Red)} \times NIR \quad (1)$$

Although the reflectance data of TROPOMI do not include a directional and atmospheric correction, the advantage of using these bands instead of similar spectral information from a different satellite sensor is that they are recorded under the same sun-sensor geometry as the SIF data. Zeng et al. (2022) similarly recommend calculating the NIRv from data that are collected from the same platform under the same illumination conditions as SIF. According to Guanter et al. (2021) these spectral bands were chosen as they show low sensitivity to atmospheric effects. The suitability of this NIRv product was evaluated against NIRv derived from BRDF-corrected MODIS reflectance bands (MCD43A4; Schaaf and Wang, 2021; see Supplementary Figs. S2 and S3).

2.2.1.3. NIRvH2. NIRvH2 was calculated according to Zeng et al. (2021). In contrast to NIRv, NIRvH2 accounts better for the soil background of mixed pixels (soil + vegetation) by using the slope in the near infrared or red region represented as k in Eq. (2) with ideally not less than three bands per region. The equation requires near infrared reflectance data in the range from 778 to 800 nm and red reflectance data at 678 nm to calculate this slope. The number of reflectance bands that are provided by the TROPOSIF L2B product are limited to two bands per region, therefore the calculation of k was performed using the bands at 773 and 781 nm. The near infrared (NIR) reflectance band at 773 nm and red (Red) reflectance band at 680 nm from TROPOSIF product were used in this study to determine NIRvH2 as follows:

$$NIRvH2 = NIR - R - k \times (\lambda NIR - \lambda R) \quad (2)$$

2.2.1.4. Additional TROPOSIF products. To account for potential hot spot effects, which can artificially increase SIF observed by TROPOMI, the phase angle was calculated from the auxiliary bands included in the TROPOSIF product (Guanter et al., 2021; Köhler et al., 2018b). The phase angle is defined as the angle between the sun and sensor as seen from the surface (Hapke, 2012). Köhler et al. (2018a) filter for phase angles between 20 and 60° which amounts to a maximum of 10% of SIF intensities at low phase angles. However, as in our dataset only 0.17% of all observations had a phase angle below 20° (at a minimum of 18.6°) no filtering was applied. To ensure data quality, observations with a cloud fraction greater than 20% were excluded using the cloud fraction band provided in the TROPOSIF product. Cloud cover is the primary limiting factor for optical satellite observations over Germany, and this threshold was selected to balance data availability and quality following the threshold applied by Wang et al. (2020a) and Zhang et al. (2019). However, it has been shown that thin clouds have little influence on SIF retrievals (Frankenberg et al., 2012; Guanter et al., 2012). Therefore, if data availability becomes limiting, relaxing this parameter could facilitate similar analyses in the future, although ΦF estimates are more reliable under clear-sky conditions. Lastly, the top of atmosphere radiance data was also gridded since it is needed for an alternative normalization scheme (cf. Section 2.3). This band is part of the

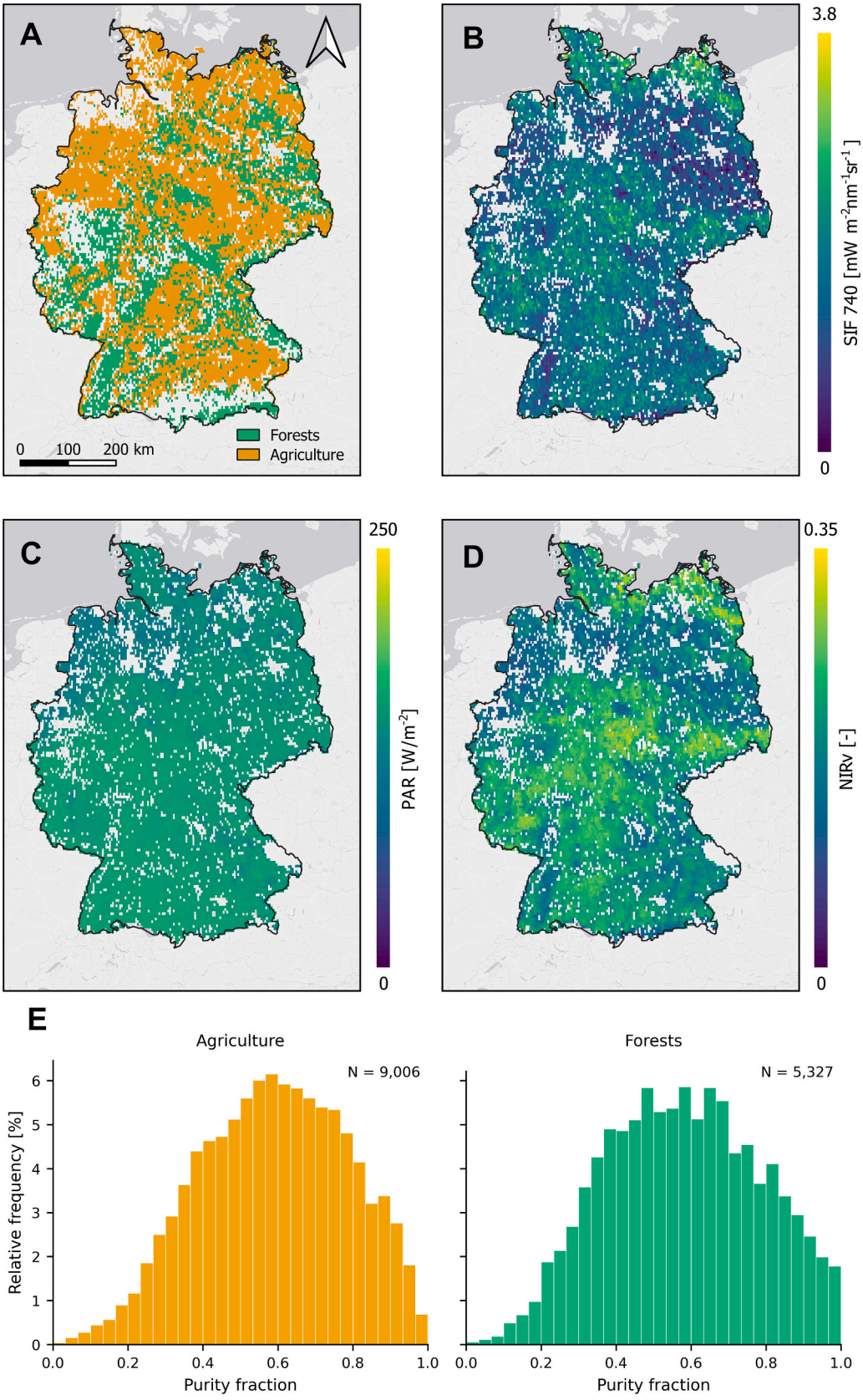

Fig. 1. Corine Land Cover (CLC) classification (A) of the two ecosystems of interest. Non-irrigated agricultural land in orange, and deciduous, coniferous and mixed forests in green. The three datasets used for the creation of the ΦF dataset shown in B, C and D (exemplary images from the 2nd of June 2019). Top of canopy SIF at 740 nm (B) and NIRv (D) from TROPOMI aboard Sentinel-5P and PAR (C) from the Breathing Earth System Simulator (BESS). E shows the distribution of within-pixel land-cover purity for agriculture and forest pixels at 0.05° resolution. Purity is defined as the fractional coverage of the target land-cover class within each pixel based on the underlying 100 m CLC dataset. (For interpretation of the references to colour in this figure legend, the reader is referred to the web version of this article.)

Table 1
Datasets used in this study, including spatial and temporal resolution.

Variable	Sensor/Model	Spatial res.	Temp. res.	Reference	Timeframe
SIF_{740}	TROPOMI	Up to 3.5 × 5.5 km	1 day	Guanter et al. (2021)	2018–2023
NIRv (Badgley et al., 2017)	TROPOMI	Up to 3.5 × 5.5 km	1 day	Guanter et al. (2021)	2018–2023
PAR	MODIS/BESS	Up to 3.5 × 5.5 km	1 day	Ryu et al. (2018)	2018–2023
Subsurface Water Storage	ParFlow/CLM	0.6 km	1 day	Beleflamme et al. (2023)	2018–2023

TROPOSIF L2B product and is the total radiance measured in the retrieval window of SIF (743–758 nm) and can be used as a proxy for PAR (Guanter et al., 2021).

Photosynthetically active radiation (PAR) and land surface temperature (LST) were used as ancillary variables in this study. PAR was obtained from the Breathing Earth System Simulator (BESS) radiation product, which provides daily estimates of incoming PAR at 0.05° spatial resolution (Ryu et al., 2018). The BESS PAR dataset is generated from MODIS atmospheric and surface information using an atmospheric radiative transfer framework combined with a machine-learning approach. Compared to the narrowband top-of-atmosphere radiance information provided by the TROPOSIF product (limited to the SIF retrieval window at 743–758 nm), the BESS PAR product should offer a more comprehensive representation of broadband light availability relevant to photosynthesis. The daily BESS PAR product was used as the radiation input for the computation of ΦF. Additionally, we evaluated the MODIS MCD18C2 PAR product for use with the instantaneous TROPOMI SIF retrievals (see Supplementary Figs. S2 and S3) (Wang et al., 2020b). However, we ultimately decided that producing ΦF at a daily temporal scale would be more useful, as it enables direct intercomparison with similar datasets in future studies. Matching the TROPOMI overpass time would require temporal interpolation of PAR, which would introduce additional uncertainty into the ΦF estimates.

LST was derived from MODIS using the MYD21C1 (Aqua) and MOD21C1 (Terra) products (Hulley and Hook, 2025). MODIS thermal infrared bands 29, 31, and 32 using the ASTER Temperature/Emissivity Separation (TES) technique are used to retrieve LST (Hulley and Hook, 2025). In our analysis, we used the LST_Day variable which the average daytime land surface temperature (K).

2.2.2. Corine land cover

The identification and masking of different land cover classes was performed using the Corine Land Cover classification CLC2018 v20 (*CORINE Land Cover 2018 (vector), Europe, 6-yearly—Version 2020_20u1, May* 2020, 2026). The classes coniferous (class 312), deciduous (class 311) and mixed forests (313) were used to define all forests in this study. This aggregation of classes was performed to increase the number of available observations and thereby improve the stability of the land-cover-specific analysis. The agricultural areas are defined as "non-irrigated arable land" (class 211), which represents the majority of agricultural areas in Germany. To better assess the representativeness of the land-cover masks at 0.05° resolution, the CLC-derived masks obtained from GEE were compared with the original 100 m CLC product. The resulting distributions of target-class purity are shown in Fig. 1E. Pixels assigned to forest and agriculture had median target-class fractions of approximately 0.58 and 0.59, respectively, indicating that both classes are strongly mixed at the 0.05° scale. In both cases, the dominant secondary contributors were the respective other class and pastures, while urban and other artificial surfaces contributed only marginally (see Supplementary Fig. S4). This analysis provides an explicit basis for interpreting the land-cover-specific results as responses of mixed landscape units rather than compositionally pure vegetation classes.

2.3. SIF normalization

Two SIF normalization methods were used in this study. Each of them normalises SIF for incoming radiation and canopy structure. The two approaches differ primarily in their temporal representation: whereas the main ΦF product is computed as a daily mean, the ΦF_R product reflects the instantaneous signal at the TROPOMI overpass time and is the only variable in this analysis that does not use the daylength scaled SIF product but only instantaneous data from TROPOMI. According to Guanter et al. (2014), Eq. (3) can be used to describe top-of-canopy (TOC) SIF as follows:

$$SIF_{canopy} = PAR \times fAPAR \times \phi F \times f_{esc} \tag{3}$$

Where PAR is the incoming photosynthetically active radiation between 400 and 700 nm, fAPAR is the fraction of absorbed PAR, ΦF is the fluorescence quantum efficiency at leaf level and fesc is the probability that a photon emitted as SIF at leaf level is leaving the canopy and thus can potentially be measured by a sensor. fAPAR and fesc are driven by canopy structural properties, and PAR and SIF describe the incoming light and fluorescence emitted at canopy scale, respectively. ΦF represents the amount of APAR that cannot be used for photosynthesis and is emitted as fluorescence corrected for canopy structural effects. ΦF serves as an indicator for the current plant physiological status and thus provides additional information about potential stress conditions (Liu et al., 2023b). By rearranging Eq. (3) ΦF can be expressed as follows:

$$\phi F = \frac{SIF_{canopy}}{PAR \times fAPAR \times f_{esc}} \tag{4}$$

To calculate ΦF based on daily available satellite data, the product of fAPAR and fesc can be approximated by NIRv according to Zeng et al., 2019 Eq. (5) shows how ΦF was determined in this study using TROPOMI canopy SIF at 740 nm, which was day-length corrected to represent daily averaged SIF and multiplied by π to approximate hemispherical SIF; NIRv calculated from TROPOMI reflectance data; and PAR data provided by the BESS PAR product, which represent daily mean PAR (see Section 2.2).

$$\phi F_{(NIRv)} = \frac{\pi \times SIF^{740}_{canopy}}{NIRv \times PAR} \tag{5}$$

The second normalization approach is using TROPOMI TOA radiance (L_{toa}) as a proxy of PAR instead of BESS PAR to test if using data from only one satellite sensor (all data from TROPOMI with the same sun-sensor geometry) provides comparable results. The SIF data used for this approach was the instantaneous SIF rather than the daily product of TROPOMI. This approach was proposed by Dechant et al. (2022) and used in a similar way by De Cannière et al. (2024) and Liu et al. (2023a). In our study, ΦF determined with this approach is called ΦF_R and was calculated as follows:

$$\phi F_{R\,(NIRv)} = \frac{\pi \times SIF^{740}_{canopy}}{NIRv \times L_{toa}} \tag{6}$$

2.4. Modelling of subsurface water storage

To assess the relationship between SIF and agricultural drought conditions, these conditions are estimated on the basis of the subsurface water storage (SSWS) anomaly which is part of the Experimental FZJ ParFlow DE06 hydrologic forecasts dataset (Belleflamme et al., 2024).

As there is no spatially and temporally continuous observational dataset at sufficiently high resolution (i.e., min ~ 5 km) providing SSWS – or any other metric representing soil moisture - over Germany, we use

model outputs generated with the hydrological model ParFlow/CLM. The ParFlow/CLM simulations used here have originally been designed to provide information on subsurface water resources at high resolution to support the agricultural sector to become more resilient against extreme hydrometeorological events (Belleflamme et al., 2023). ParFlow is an integrated, physics-based hydrological model that simulates the 2D surface and 3D variably saturated subsurface water states and fluxes (Kuffour et al., 2020). We use it with its internal land surface module CLM (Common Land Model), which calculates the energy and water exchange at the land surface, i.e., the atmosphere-vegetation-subsurface interface (Dai et al., 2003). Here, ParFlow/CLM is deployed at 611 m resolution over a domain covering Germany and its surrounding regions and it is run at an hourly time step. It has 15 vertical layers reaching from the surface to 60 m depth with a thickness increasing with depth to better resolve the highly dynamic processes close to the surface. The topography is based on the ASTER DEM (Digital Elevation Model) (Abrams et al., 2020) and the hydrological network is corrected with the hydrologically adjusted MERIT DEM (Yamazaki et al., 2019). The land cover is parametrized with the Corine Land Cover CLC2018 v20 (*CORINE Land Cover 2018 (vector), Europe, 6-yearly—Version 2020_20u1, May* 2020, 2026) converted into the 18 IGBP (International Geosphere-Biosphere Programme) classes. For the parametrization of the soil hydraulic properties above the depth to bedrock, the SoilGrids250m v2017 (Hengl et al., 2017) soil texture is reclassified to the 12 USDA textural classes for which the ROSETTA pedotransfer function parameters (porosity, saturated hydraulic conductivity, Van Genuchten parameters; Schaap et al., 2001) are used. Below the depth to bedrock, we use the six hydrogeological types from the International Hydrogeological Map of Europe (IHME1:1,500,000; Duscher et al., 2015). The atmospheric forcing comes from the deterministic high-resolution weather forecast HRES from ECMWF (European Centre for Medium-Range Weather Forecasts) (Owens and Hewson, 2018), from which the first 24 h of each daily forecast are used. A detailed description of this setup as well as an evaluation of the model results can be found in Belleflamme et al. (2023). The evaluation shows that the ParFlow/CLM simulations at a monthly timescale are able to reproduce the spatial and temporal dynamics of observational data for soil moisture, evapotranspiration, groundwater table depth, and riverine discharge. In particular, a comparison with ESA-CCI volumetric soil moisture for the uppermost model layer (0–2 cm depth) yields results for the temporal Pearson correlation of the same order of magnitude than the ERA-Interim reanalysis from ECMWF, and the root-mean-square error of the anomalies lies below the uncertainty of the ESA-CCI volumetric soil moisture (Belleflamme et al., 2023).

Here, we define SSWS as the water column stored in the subsurface. This has the advantages over, e.g., volumetric soil moisture, soil water saturation, or plant available water, which all provide the same information but with different units, that it can be easily aggregated over several model depth layers and it gives the amount of water in the soil without needing additional information on the soil hydraulic properties, such as the porosity, the field capacity, etc.

As in this study we investigate the relationship between the variations of SSWS and SIF over time, we consider SSWS anomalies, which allows us to circumvent model-internal systematic biases in the SSWS data (Fig. 2). For each day d, the anomaly is calculated with regard to the long-term 31-day average around that day (i.e., from d-15 to d + 15) over the 10-year period 2013–2022, thereby filtering out the seasonal cycle.

Throughout this study, the SSWS layer spanning 0.10–0.17 m is used to represent water availability conditions relevant for vegetation dynamics. This depth lies at the transition between surface soil moisture and root zone soil moisture and thus provides a compromise between the rapid variability of near-surface layers and the delayed response of deeper soil layers (Li et al., 2023b). Layers closer to the surface are strongly coupled to short-term atmospheric forcing (precipitation and evapotranspiration), resulting in rapid wetting–drying cycles that can obscure the identification of sustained drought development. In contrast, deeper layers respond more slowly to changes in meteorological forcing because of their higher inertia, which can delay the detectable onset of agricultural drought. In addition, uncertainty

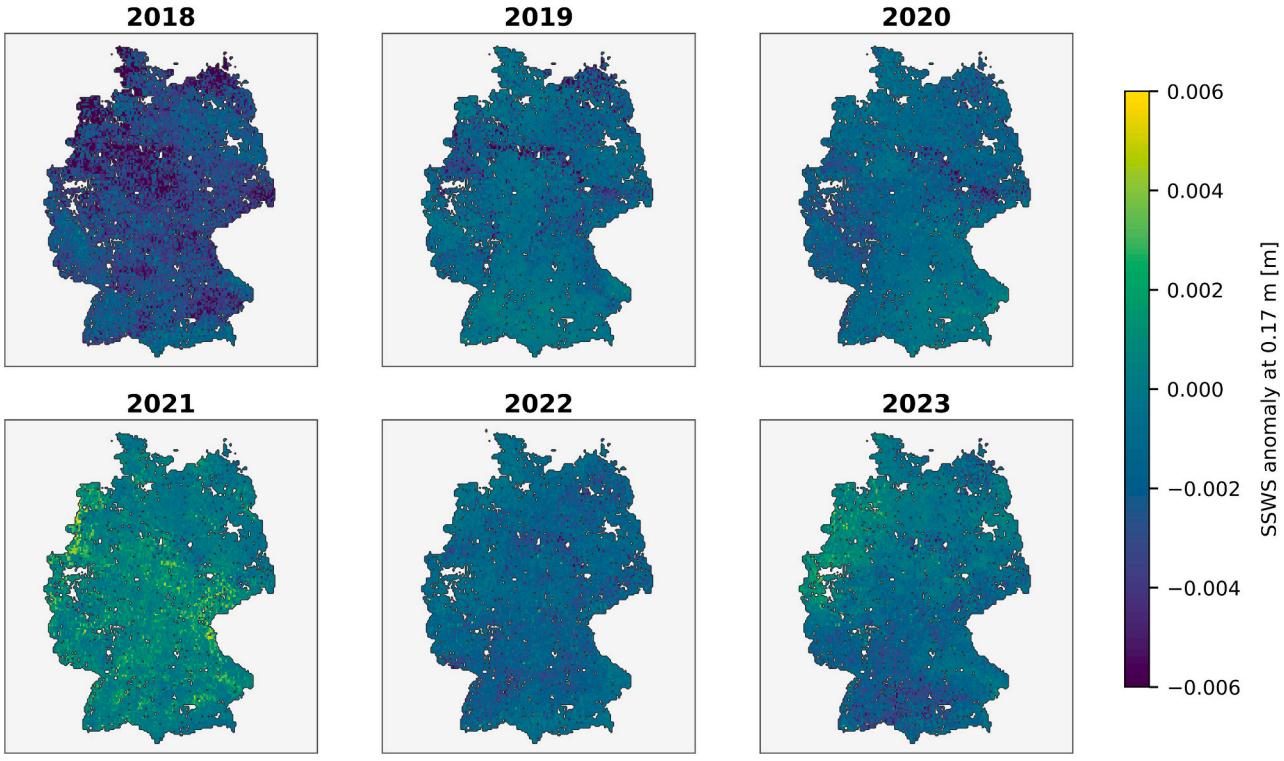

Fig. 2. Subsurface Water Storage Anomaly at 0.17 m averaged per year in Germany of all pixels classified as natural surfaces, simulated with the hydrological model ParFlow/CLM.

increases with depth as subsurface parameterization exerts a stronger control relative to atmospheric boundary conditions. While deeper root zone soil moisture may be more directly linked to vegetation drought stress, this study focuses on agricultural drought dynamics and the lagged response of remotely sensed indicators to soil moisture anomalies during drought periods. As the remotely sensed indicators used here are derived from surface observations, the selected layer serves as a pragmatic reference depth that remains linked to surface-driven anomalies while being less affected by very short-term fluctuations in the uppermost soil layers. This choice is not intended to represent the exact effective root-zone depth of all vegetation types, but rather to provide a common reference depth for comparing remotely sensed surface signals with simulated soil moisture anomalies.

2.5. Data processing and workflow summary

To handle the large amounts of data involved in this study, the majority of processing was performed in Google Earth Engine using its Python API. Before the data could be uploaded to Google Earth Engine (GEE) using GEEup (Roy, 2025), several preprocessing steps were applied.

The SSWS and SSWS anomaly (SSWSa) data was remapped to 0.05° using the climate data operator (CDO) (Schulzweida, 2023). Then the data was exported into individual.tiff file per day which were reprojected to WGS84. Preprocessing of TROPOSIF started by gridding the L2B data including SIF740, the reflectance and TOA radiance bands as well as all auxiliary bands to 0.05° and exporting them as daily.tiff files. Both datasets could then be uploaded to individual legacy assets in GEE using GEEup.

Within GEE, NIRv as well as the phase angle were calculated using the reflectance and auxiliary bands from TROPOMI. Both mentioned normalization methods were performed and masked by cloud fractional cover and phase angle. The BESS PAR (with the exception of the years 2022 and 2023, which needed to be uploaded using GEEup) and LST datasets were already available in GEE and could be integrated at this step into the workflow. The SIF and PAR data were then used to mask the SSWS and SSWSa data to ensure a perfect match between all datasets. The data were then split into different bands corresponding to the mentioned CLC land cover classes before they could be exported as separate.tiff files for each day and each variable.

The workflow, starting with the sensor-provided data and ending with the final products ΦF and SSWS/SSWSa used for comparison, is illustrated in Fig. 3. The final data masking was applied to all other variables against which ΦF and SSWSa were compared to, including top of canopy SIF, NIRv, NDVI, NIRvP, ΦF_R, PAR and LST. To create a global dataset to detect the relationships between the different data products,

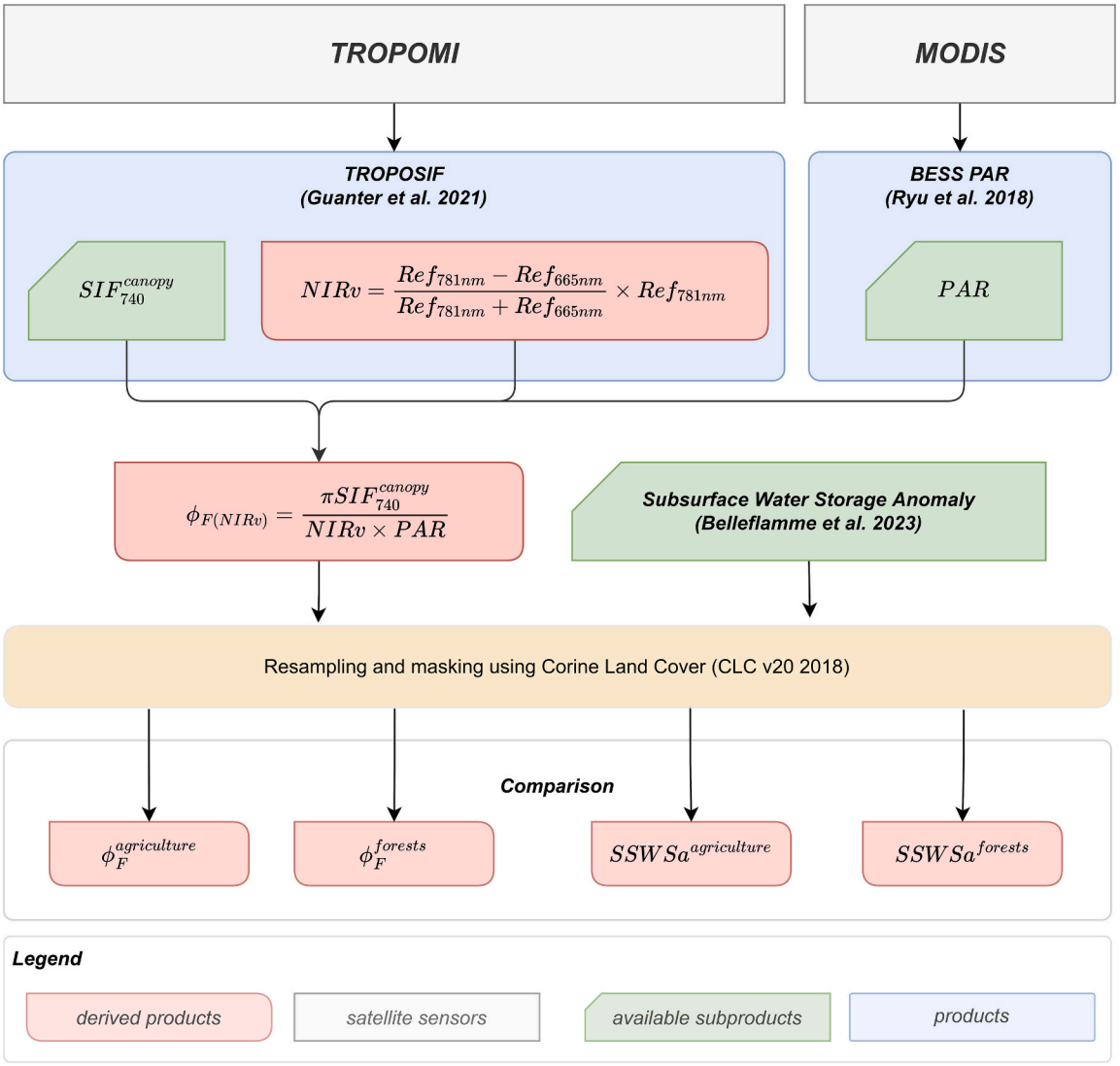

Fig. 3. Flowchart showing the satellite products involved in calculating ΦF and the postprocessing steps involved for the subsequent comparison to SSWSa.

the median for each day and product was calculated and then averaged again using rolling averages from two to six days.

2.6. Statistical analysis

The comparison of ΦF and other variables to SSWSa was performed using cross-correlation coefficients at different lags. Cross-correlation coefficients were calculated for each time series at lag 0 which corresponds to the data being compared at the same day. The target time series was then shifted into the future by one day until the maximum number of lags were reached (7 days). The change in cross-correlation coefficient gives insight into a potential lag of one time series over the comparison time series of SSWSa. A maximum lag of 7 days was specified, as any lag between ΦF and SSWSa was expected to occur within this period. For each variable, the resulting cross-correlation functions were then averaged across all detected drought periods. Additionally, significance of the found cross-correlation patterns was evaluated using a surrogate-based Monte-Carlo approach. For each drought period and variable, surrogate time series were generated using a moving block bootstrap with a block length of 5 days to preserve temporal autocorrelation while destroying temporal alignment with SSWS anomalies. Cross-correlation functions were computed for each surrogate and compared with the observed cross-correlation to assess significance at different lags. A total of 1000 surrogate realizations was generated for each drought period and variable. From the surrogate distribution, pointwise 95% envelopes were derived for each lag and included in the resulting plots as an autocorrelation-aware null reference. The associated 95% envelopes are included in the resulting plots. This methodology was partially adapted from Vitale et al. (2024). While this approach cannot prove causal linkages, it helps to rule out that the observed lagged cross-correlation patterns arise solely from the time-series persistence (autocorrelation) of the variables.

3. Results

To assess whether ΦF can serve as an early indicator of drought stress, drought periods were first identified from the full time series before subsequent temporal aggregation and regional subsetting were applied.

3.1. Selection of drought periods

The SIF, NIRv and PAR time series of all observed vegetation periods show an expected seasonal pattern characterised by increasing values until June/July followed by decreasing values toward autumn (Fig. 4). Especially NIRv and SIF show a very similar seasonal trend, underlining that both parameters provide similar information about canopy structure and total canopy chlorophyll content. Since ΦF is normalized for canopy structure and illumination effects, this seasonality is much reduced in the ΦF time series.

A comparison between the variables involved in the calculation of ΦF is shown in Fig. 5. NIRv in relation to SIF shows high R^2 of 0.89 and 0.81 for agriculture and forest ecosystems respectively which is supported by literature that SIF is strongly influenced by canopy structure (Fig. 5, A, B) (Dechant et al., 2020). This is supported by the low linear correlation between SIF and PAR (0.36 for both ecosystems) (Fig. 5, C, D) suggesting that canopy structure, which modulates the SIF signal, does not respond directly to short-term fluctuations in PAR.

The reason why, we do not see saturated SIF signal under high PAR conditions is likely related to the size of the TROPOMI pixels and the averaging that is applied to the data. As each data point represents the median value of all available pixels, any outliers are simply not visible within the data.

There are periods in 2018 and 2022 in which ΦF shows large variations. These effects are caused by low PAR values as a result of high cloud coverage and thus sparse data availability. SSWSa is mainly negative in 2018 and 2022. The years 2019 and 2020 show predominantly periods of negative anomalies interrupted by short periods characterised by positive values. In contrast, in 2021 SSWSa is continuously positive (except a short period in June) because the year was abnormally wet. The year 2023 shows positive SSWSa values in spring followed by negative values during summer. Since negative SSWSa values indicate insufficient water supply (Belleflamme et al., 2023), the presented time-series agrees with literature, that 2018, 2019, 2020 and 2022 were years heavily affected by drought events in Germany (Belleflamme et al., 2023; Bevacqua et al., 2024).

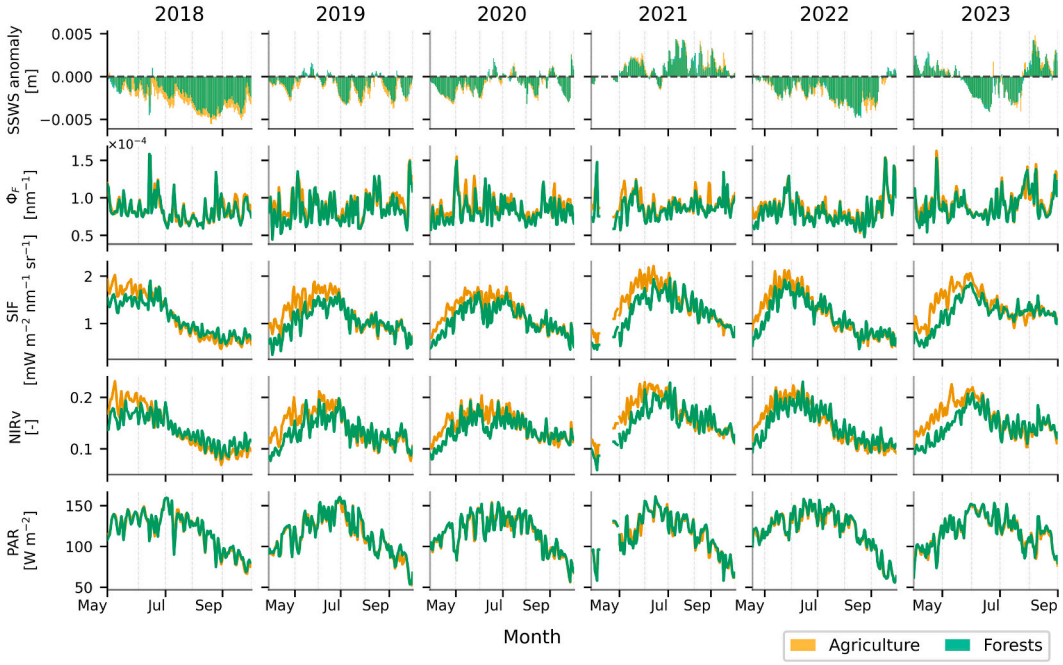

Fig. 4. Time series of SSWSa (0.17 m), ΦF, SIF, NIRv and PAR for the vegetation periods (March–October) of the years 2018–2023. The time series represent averaged values for all agricultural areas and forests in Germany using a two-day rolling average.

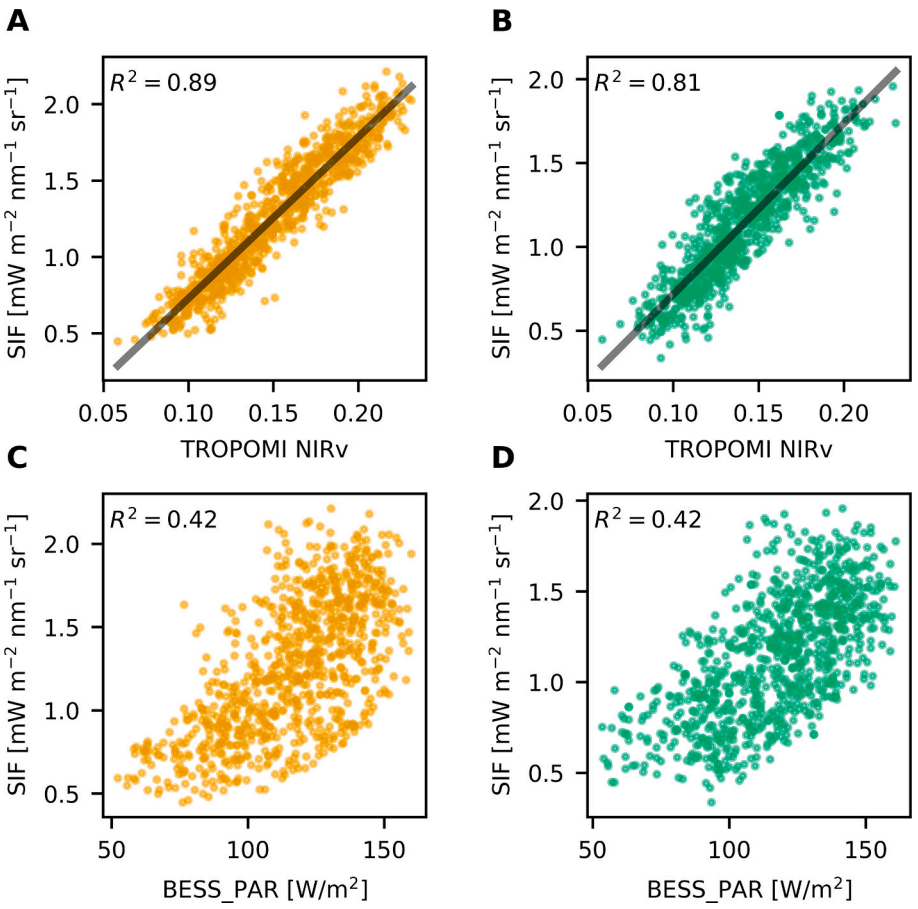

Fig. 5. Correlation of the variables involved in the calculation of ΦF for agriculture (A, C in orange) and forests (B, D in green). (For interpretation of the references to colour in this figure legend, the reader is referred to the web version of this article.)

Selecting severe drought periods was done using the SSWSa time series data sets of agricultural and forest areas. A period was defined as a drought period when the SSWSa was negative for at least 30 days in a row. The time periods identified shown in Fig. 6 for the two ecosystems differ in length because they are represented by a different amount of pixels and a different geographic location, and therefore they have

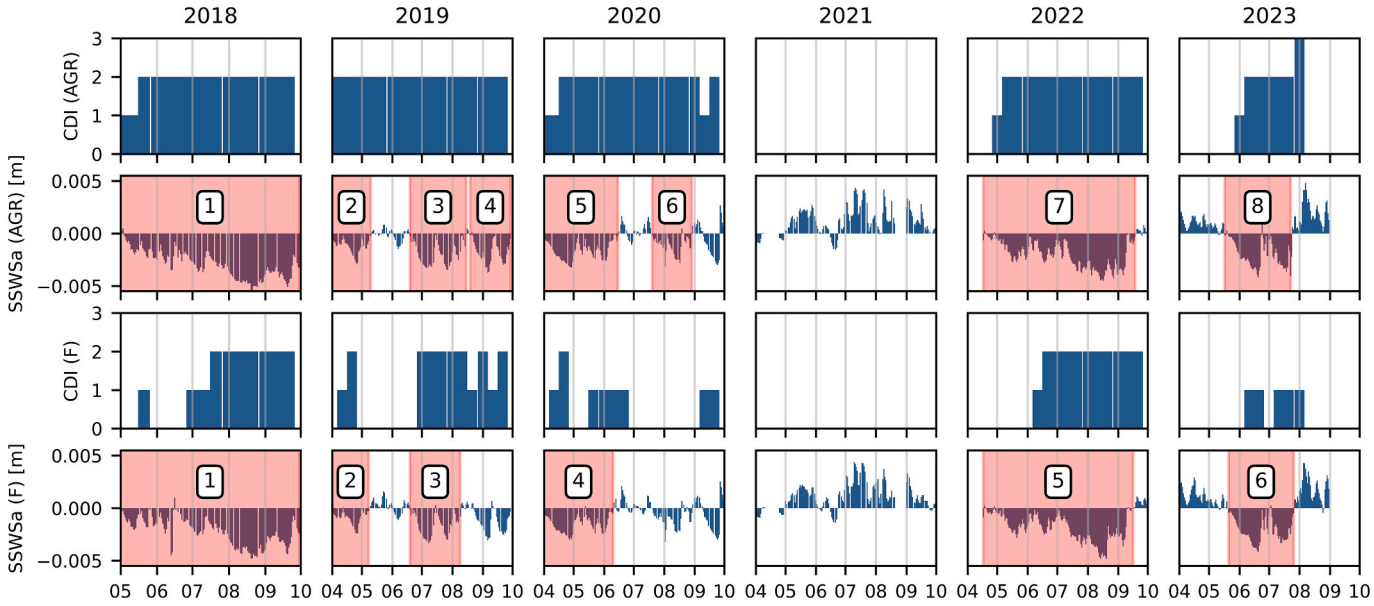

Fig. 6. Selected drought periods (subframes marked in red) based on periods of negative SSWSa values at 0.17 m soil depth lasting longer than 30 days. Top panels show the SSWSa and linked CDI classification of agricultural areas, bottom panels show the SSWSa and CDI classifications for forests. (For interpretation of the references to colour in this figure legend, the reader is referred to the web version of this article.)

different SSWSa values.

All selected drought periods were checked for conformity with watch (periods of precipitation deficit) and warning (negative soil moisture anomaly) periods identified by the CDI (European Commission, Joint Research Centre (JRC) (2022)) (Fig. 6). The length of the drought periods, referred to as subframes in the further course of this study, varies from 34 to 152 days. The periods cover the drought years of 2018, 2019, 2020, 2022 and the summer of 2023. The analysis was purposefully not split into long time periods such as 2018 and 2022 and shorter periods to gain a first general understanding if and how ΦF is able to track changes in SSWSa.

3.2. *Determining the optimal temporal aggregation for comparing ΦF and subsurface water storage anomaly*

This subsection evaluates the sensitivity of lagged ΦF–SSWSa cross-correlation patterns to ΦF temporal averaging. A major limitation of optical data in central Europe is cloud cover. We therefore only have ~38.9 and 38.1% median coverage during drought periods for agriculture and forest land cover respectively. To mitigate this, a rolling average is applied to the time series. Temporal aggregation directly affects both the detectability and robustness of lagged ΦF–SSWSa relationships. To quantify this trade-off, we compared rolling averages of ΦF from 2 to 6 days with respect to the strength and clarity of the lagged cross-correlation signal and the spatial coverage of valid observations. Across all averaging windows, the cross-correlation functions exhibit a similar short-lag response structure, with increasing coefficients during the first few days followed by a decline at longer lags (Fig. 7, A, B). However, the exact location of the peak changes slightly with the length of the averaging window. In particular, longer averaging windows tend to smooth the curves and shift the correlation maximum somewhat toward later lags, while also increasing the overall magnitude of the cross-correlation. The variability across drought periods, expressed by the standard deviation (Fig. 7, C, D), tends to increase with increasing averaging window length. Nevertheless, the 2-day average preserves a comparatively clear early peak structure while already improving spatial coverage relative to unsmoothed data. At the same time, spatial coverage increases with longer averaging windows due to a higher number of available observations (Table 2). Considering both temporal interpretability and spatial coverage, the 2-day rolling average provided the best compromise between preserving an early and clearly defined lag structure and improving the number of valid observations, whereas longer averaging windows increasingly shifted the peak toward later lags and were associated with higher standard deviation. We therefore used the two-day rolling average for all subsequent analyses to maximize sensitivity to early drought stress while maintaining robust spatial representativeness.

Table 2
Percentages of median available pixels during the identified drought periods for agricultural and forested areas with increasing number of days included in the rolling average calculation.

Rolling Average [days]	1	2	3	4	5	6
Agriculture [%]	38.9	55.3	67.4	75.7	82	86.3
Forests [%]	38.1	55.3	67	75.6	82.2	86.1

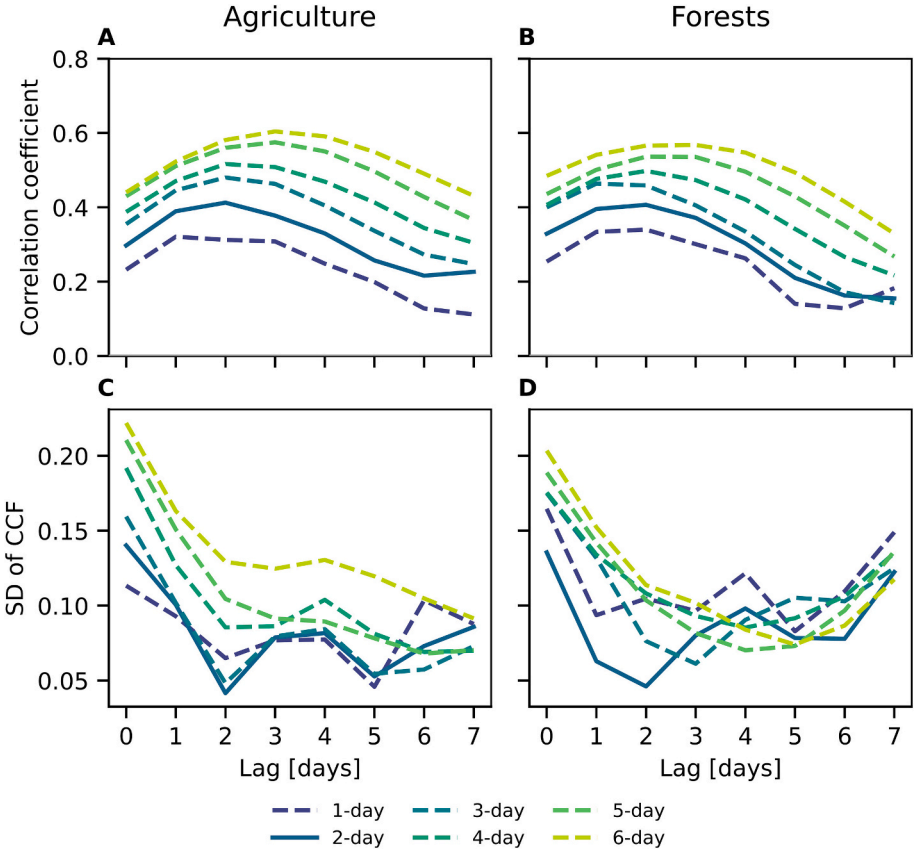

Fig. 7. Cross-correlation coefficients between Φ_F and SSWSa calculated using temporal rolling-average windows of 1–6 days for (A) agriculture and (B) forests. Panels (C) and (D) show the corresponding standard deviation (SD) of the cross-correlation coefficients across drought periods for agriculture and forests, respectively. The different line colours indicate the applied rolling-average window length.

3.3. Comparison of subsurface water storage anomaly with selected remote sensing satellite products

Following the identification of severe drought periods and the optimal temporal averaging, cross-correlation coefficients can now be computed between SSWSa and other remote sensing-based variables considered to be important for detecting drought stress across both land cover types.

SSWSa was compared to three different groups of variables: i) the fluorescence-based variables SIF, ΦF and ΦF_R, ii) vegetation indices NIRv, NDVI and NIRvP, and iii) LST and PAR. NIRvH2 was excluded from this comparison as it showed to be near identical to NIRv. A comparison between the two variables was added to the supplementary (see Fig. S1).

For agricultural areas (Fig. 8, Table 3) all vegetation indices (NDVI, NIRv and NIRvP) show the same concave pattern of low positive correlation coefficients at the beginning and at the end and slightly negative values in the middle of the considered lag range. Furthermore, all indices are characterised by high standard deviations. Furthermore, all observed correlations remain within the surrogate-based Monte-Carlo confidence envelope across the considered lag range, indicating that this pattern is not statistically significant once temporal autocorrelation is accounted for. These results indicate that decreasing SSWSa has no impact on the indices within the observed period of seven days. Multiplying PAR with NIRv to calculate NIRvP does also not appear to make a significant difference.

Among the SIF variables, differences are much more obvious. Top of canopy SIF and ΦF_R are showing the highest cross-correlations at the beginning, similar to the vegetation indices but ΦF_R has a lower standard deviation compared to top of canopy SIF. The correlation coefficients of both variables are relatively small, which indicates that they are not sensitive to SSWSa within the period of interest. The cross-correlations for SIF and ΦF_R are slightly positive at the beginning and then drop to zero after 2 and 5 days, respectively. Consistent with this weak response, their correlations exceed the surrogate-based Monte-Carlo envelope only at the earliest lags, indicating that any association with SSWSa is limited and not persistent over the considered periods. In contrast, ΦF has a relatively low standard deviation and a clearly pronounced pattern characterised by an increasing positive cross-correlation coefficient reaching its peak after 2 days followed by decreasing values until the end of the observation period. ΦF remains outside of the Monte-Carlo envelope across most lags, confirming a robust lagged response to decreasing SSWSa with a peak correlation coefficient of 0.38 after 2 days. The low standard deviation illustrates the sensitivity of ΦF to decreasing levels of SSWSa. The comparison of PAR to SSWSa reveals an inverse relationship represented by negative correlation values which exceed the significance envelope at lag 1–6. The standard deviation is relatively high, and the highest correlation coefficient was determined for a lag of 3 days. The temporal trend in the correlation coefficients of LST is very similar to that of ΦF but shows an inverse behaviour. This means a decrease in SSWSa is causing an increase in LST. The highest negative correlation coefficient can be observed after 1 day and the standard deviations are on a moderate level. LST also exceeds the significance envelope across all lags. The correlation coefficients and standard deviation for each variable are shown in Table 3. The high correlations found for LST (−0.48) and ΦF (0.38) emphasize that these two remote-sensing parameters respond most sensitive to decreasing SSWSa values while also expressing a similar response pattern with a lag of 1 to 2 days.

The cross-correlation trends for all variables in the land cover class forests are similar to those determined for the land cover class agricultural area. This similarity is consistent with the quantified subpixel composition of the masks (Section 2.1, Fig. 1, E), which showed that both land-cover subsets are strongly mixed at 0.05° resolution. However, a few distinct deviations are clearly visible (Fig. 9, Table 4). Again, the vegetation indices show no correlation with SSWSa and their trends

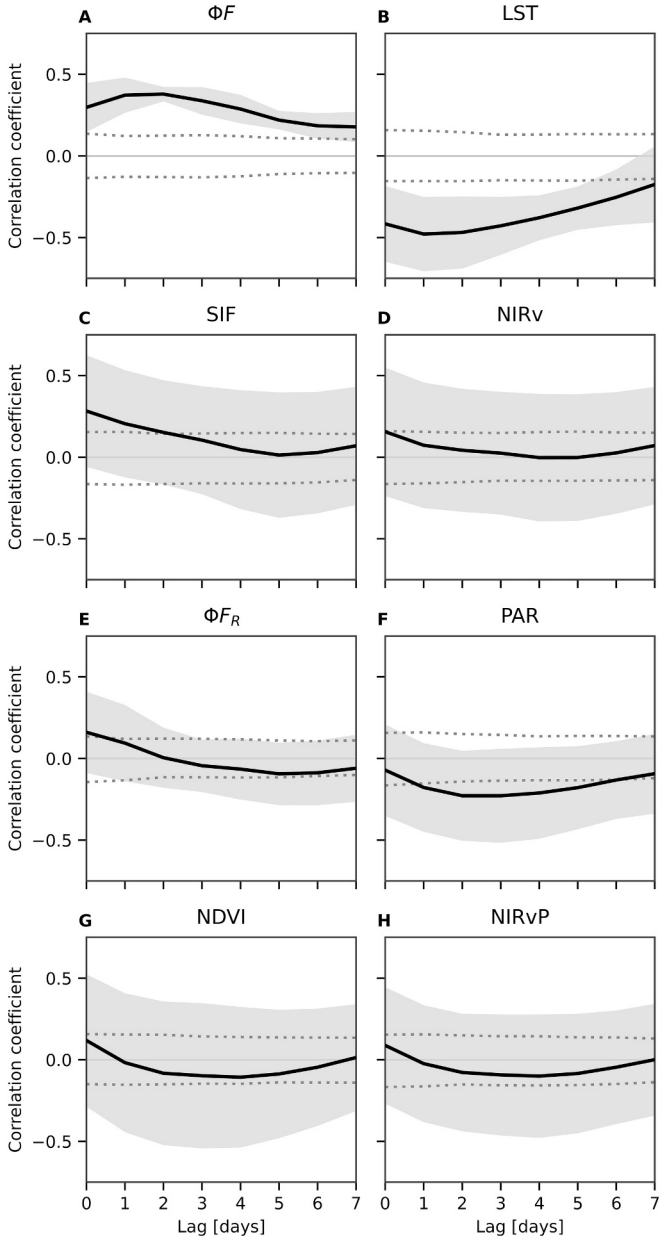

Fig. 8. Cross-correlation analysis for the land cover class agriculture. The black lines represent the averaged cross-correlation coefficients determined for SSWSa and different remote sensing satellite products (ΦF, LST, SIF, NIRv, ΦF_R, PAR, NDVI, and NIRvP) for all agricultural areas in Germany covering a range of lags from 0 to 7 days, while the grey marked areas illustrate the corresponding standard deviations. The dotted lines show the MC simulated confidence envelope of 95%.

are characterised by high standard deviations. In agreement with this, the cross-correlation coefficients remain within the surrogate-based Monte-Carlo confidence envelope across the considered lag range. For top of canopy SIF, the highest correlation coefficient is present in the beginning accompanied by a relatively high standard deviation that further increases with the number of observation days. These correlations remain largely within the confidence envelope, suggesting at most a weak and short-lived association with SSWSa. In general, ΦF_R has lower correlation coefficients compared to SIF, while ΦF shows a very similar pattern as the one of ΦF for agricultural areas with an equally lower standard deviation throughout all lags. The highest cross-correlation coefficient of 0.38 after 1 day is also similar to the one determined for agricultural areas (0.37) while the standard deviation

Table 3
Averaged cross-correlation coefficients and corresponding standard deviations determined for SSWSa and different remote sensing satellite products (SIF, ΦF, $ΦF_R$, NIRv, NDVI, NIRvP, PAR and LST) for all agricultural areas in Germany covering a range of lags from 0 to 7 days. Highest correlation coefficient for each variable highlighted in bold.

Variable	*Lag 0*	*Lag 1*	*Lag 2*	*Lag 3*	*Lag 4*	*Lag 5*	*Lag 6*	*Lag 7*
SIF	**0.28 ± 0.34**	0.21 ± 0.33	0.15 ± 0.32	0.1 ± 0.33	0.05 ± 0.36	0.01 ± 0.38	0.03 ± 0.37	0.07 ± 0.36
NIRv	**0.16 ± 0.39**	0.07 ± 0.38	0.04 ± 0.38	0.02 ± 0.38	−0.0 ± 0.39	−0.0 ± 0.39	0.03 ± 0.37	0.07 ± 0.36
PAR	−0.07 ± 0.28	−0.18 ± 0.27	**−0.23 ± 0.28**	−0.23 ± 0.29	−0.21 ± 0.28	−0.18 ± 0.25	−0.13 ± 0.24	−0.09 ± 0.24
ΦF	0.3 ± 0.15	0.37 ± 0.11	**0.38 ± 0.04**	0.34 ± 0.08	0.29 ± 0.09	0.22 ± 0.06	0.18 ± 0.08	0.18 ± 0.09
NDVI	**0.12 ± 0.41**	−0.02 ± 0.43	−0.08 ± 0.44	−0.1 ± 0.44	−0.11 ± 0.43	−0.09 ± 0.39	−0.05 ± 0.36	0.01 ± 0.33
LST	−0.42 ± 0.23	**−0.48 ± 0.23**	−0.47 ± 0.22	−0.43 ± 0.18	−0.38 ± 0.14	−0.32 ± 0.13	−0.25 ± 0.17	−0.17 ± 0.23
$ΦF_R$	**0.16 ± 0.25**	0.09 ± 0.23	0.0 ± 0.18	−0.04 ± 0.16	−0.07 ± 0.19	−0.09 ± 0.19	−0.09 ± 0.2	−0.06 ± 0.21
NIRvP	0.09 ± 0.36	−0.02 ± 0.36	−0.08 ± 0.36	−0.09 ± 0.37	**−0.1 ± 0.38**	−0.08 ± 0.37	−0.05 ± 0.35	0.0 ± 0.34

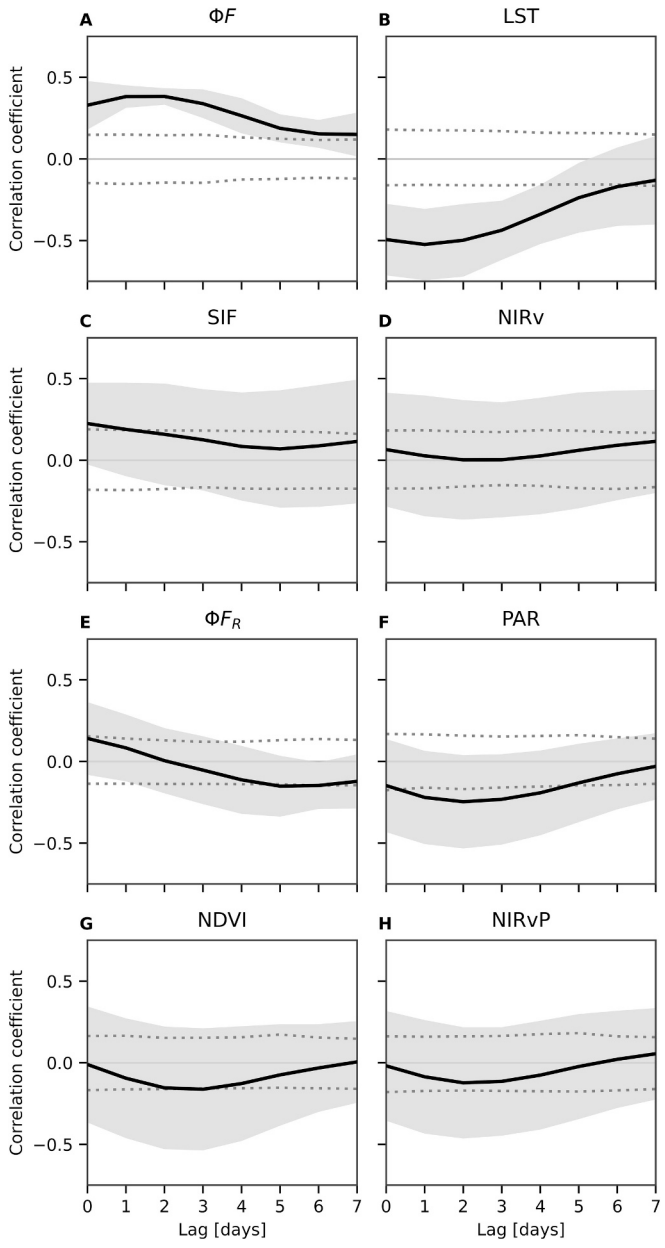

Fig. 9. Cross-correlation analysis for the land cover class forest. The black lines represent the averaged cross-correlation coefficients determined for SSWSa and different remote sensing satellite products (ΦF, LST, SIF, NIRv, $ΦF_R$, PAR, NDVI, and NIRvP) for all forest areas in Germany covering a range of lags from 0 to 7 days, while the grey marked areas illustrate the corresponding standard deviations. The dotted lines show the MC simulated confidence envelope of 95%.

with 0.07 is slightly reduced. ΦF consistently exceeds the Monte-Carlo envelope across all lags, confirming a robust and temporally coherent response to decreasing SSWSa in forests. The negative correlation coefficient for the vegetation independent variable PAR is peaking after 2 days and then continuously decreases. The standard deviation of PAR is on a stable high level throughout the entire observation period and is within the Monte-Carlo envelope from lag 4 onward. Similar to agricultural areas, LST of the land cover class forest shows high negative cross-correlation coefficients for the first few days followed by a decline with relatively low standard deviations. LST remains outside the confidence envelope for the considered lag range, supporting a consistent thermal response to soil moisture deficits. The similar responses of ΦF and LST in both land-cover classes are most plausibly explained by mixed-pixel effects, as the 0.05° resolution in combination with the discrete classification of the CLC dataset inevitably leads to pixels that contain multiple land-cover types. Fragmentation within the land-cover classification likely further enhances this mixing. The results of the cross-correlation analysis for both land cover classes clearly reveal that decreasing levels of SSWSa lead to changes in ΦF and LST after a lag of 1–2 days and to a certain extent this is also visible in changing PAR values. For this reason, the subsequent analysis focussing on the different drought subframes and the comparison of entire Germany to the eastern part of Germany will be solely based on ΦF and LST.

3.4. Regional comparison of subsurface water storage anomaly to ΦF

To better understand the relationships identified for Germany as a whole between ΦF, LST and SSWSa, the same methodology was applied to a spatial subset of the federal states of Saxony-Anhalt and Brandenburg. Both states were strongly affected by droughts during the study period (German Environment Agency, 2024). While the strong aggregation over the entire country already revealed a connection of ΦF to SSWSa, the regional analysis could more directly show if this pattern is in fact detectable in regional drought conditions. It could also help in understanding if and how ΦF could be used as a drought indicator at finer spatial scale. The results show an increase in cross-correlation for ΦF followed by a drop after 2 days and an inverse pattern for LST in agricultural areas (Fig. 10). These patterns for both LST and ΦF align with the findings on the national level, though the standard deviation is slightly higher.

In contrast, forested areas in the eastern subset display a much weaker signal compared to the national average. Relatively high standard deviation and an almost constant cross-correlation coefficient around 0.25 and − 0.25 for ΦF and LST respectively only exhibit a slight change from 0 to 2 days of lag while at the same time only slightly exceeding the Monte-Carlo significance envelope across all lags (see Supplementary S5). The individual subframes of the forested areas reflect the lack of pattern visible in the averaged cross-correlation, with some subframes even showing positive correlations for LST to SSWSa. Overall, these results suggest that the connection observed at national level still persists in agricultural areas, while in forests the pattern disappears. Since the pattern weakens for both LST and ΦF, a likely

Table 4
Averaged cross-correlation coefficients and corresponding standard deviations determined for SSWSa and different remote sensing satellite products (SIF, ΦF, $ΦF_R$, NIRv, NDVI, NIRvP, PAR and LST) for all forest areas in Germany covering a range of lags from 0 to 7 days. Highest correlation coefficient for each variable highlighted in bold.

Variable	Lag 0	Lag 1	Lag 2	Lag 3	Lag 4	Lag 5	Lag 6	Lag 7
SIF	**0.22 ± 0.25**	0.19 ± 0.29	0.16 ± 0.31	0.12 ± 0.31	0.08 ± 0.33	0.07 ± 0.36	0.09 ± 0.37	0.11 ± 0.38
NIRv	0.06 ± 0.35	0.03 ± 0.37	0.0 ± 0.37	0.0 ± 0.35	0.03 ± 0.36	0.06 ± 0.35	0.09 ± 0.34	0.12 ± 0.32
PAR	−0.15 ± 0.28	−0.22 ± 0.29	**−0.25 ± 0.29**	−0.23 ± 0.28	−0.19 ± 0.26	−0.13 ± 0.24	−0.08 ± 0.22	−0.03 ± 0.2
ΦF	0.33 ± 0.15	**0.38 ± 0.07**	**0.38 ± 0.05**	0.34 ± 0.09	0.26 ± 0.11	0.19 ± 0.09	0.15 ± 0.09	0.15 ± 0.13
NDVI	−0.01 ± 0.36	−0.09 ± 0.37	−0.15 ± 0.38	**−0.16 ± 0.37**	−0.13 ± 0.35	−0.07 ± 0.31	−0.03 ± 0.27	0.01 ± 0.25
LST	−0.49 ± 0.22	**−0.52 ± 0.22**	−0.5 ± 0.22	−0.44 ± 0.18	−0.34 ± 0.18	−0.24 ± 0.21	−0.17 ± 0.24	−0.13 ± 0.27
$ΦF_R$	**0.14 ± 0.22**	0.08 ± 0.2	0.0 ± 0.2	−0.05 ± 0.21	−0.11 ± 0.21	−0.15 ± 0.19	−0.15 ± 0.14	−0.12 ± 0.17
NIRvP	−0.02 ± 0.34	−0.09 ± 0.35	**−0.12 ± 0.34**	−0.11 ± 0.33	−0.08 ± 0.33	−0.02 ± 0.32	0.02 ± 0.3	0.06 ± 0.28

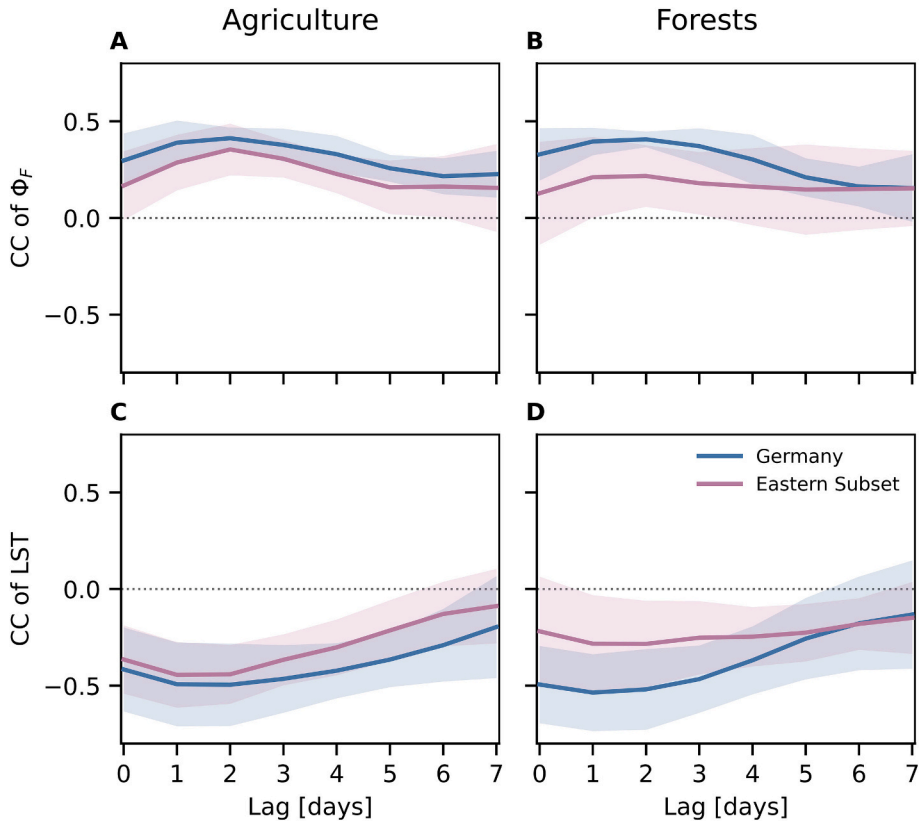

Fig. 10. Cross-correlation function of ΦF and LST to SSWSa at different lags for biomes agriculture (A, C) and forests (B, D) in all of Germany and Saxony-Anhalt and Brandenburg combined ("Eastern Subset"). Averages shown with standard deviation per variable and region of interest.

explanation is reduced data availability and increased uncertainty in the regional forest subset, although a region-specific difference in the aggregated response cannot be excluded. This regional response needs to be further investigated in areas with higher data availability to further explore the connection of ΦF to SSWSa.

4. Discussion

4.1. Normalization of SIF and generating a ΦF time-series

In this study, we used TROPOMI and MODIS based BESS PAR satellite data to normalize SIF for canopy structure and illumination conditions, ultimately generating a multi-year (2018–2023) ΦF dataset for all of Germany. This dataset was analyzed to investigate the potential of a ΦF time-series to be suited for detecting early signs of drought stress. The normalization approach adapted from Liu et al. (2023a) was successfully transferred to GEE and thus allowed us to generate a ΦF time series for Germany covering six vegetation periods. The time series can also be extended into the future as long as the L2B TROPOSIF products and corresponding BESS PAR data are available. Creating a ΦF time series at daily temporal resolution requires calculating NIRv as a proxy of the product of fAPAR and fesc. However, NIRv is not entirely consistent with radiative transfer theory and not suited for pixels having low fractional vegetation cover (Yang et al., 2020). For this reason, in future studies NIRv could be replaced by other indices such as FCVI (Yang et al., 2020) or NIRvH (Zeng et al., 2021). This comes with the limitation that these indices require hyperspectral TOC reflectance data that are not provided by TROPOMI but possibly by future satellites. The cross-correlation patterns and trends identified suggest that the extensive spatial aggregations applied in this study render these potential errors negligible. It was also tested if TOA radiance can be used as a proxy for PAR as suggested in De Cannière et al. (2024) and Guanter et al. (2021). The benefit of following this approach is that the sun-sensor geometry of all measured remote sensing variables would be the same allowing for the calculation of instantaneous ΦF. The results, however, do not show any meaningful correlation or pattern, which may

be due to the fact that TOA radiance from TROPOMI only covers the retrieval window of 743–758 nm, rather than the full PAR range of 400–700 nm important for photosynthesis related processes.

A validation of our ΦF product can most likely only be achieved after the launch of the FLEX satellite mission in 2026 (ESA, 2025). FLEX will operate in a tandem constellation with Sentinel-3. Together, the FLORIS instrument aboard FLEX and the OLCI instrument aboard Sentinel-3 will provide all information necessary to accurately determine SIF, fesc and fAPAR to eventually calculate ΦF. The GSD of 300 m will allow for in situ validation, which has been shown to be challenging for currently available satellite SIF products with GSDs ranging from ~1 km (OCO-2) to ~5 km (TROPOMI) GSD (Du et al., 2023). Although FLEX's 27-day revisit time limits its use for operational drought monitoring, FLEX ΦF products can be compared to our ΦF product in the form of a satellite intercomparison. Furthermore, integrating FLEX ΦF products into our ΦF time series offers the potential for smaller-scale studies that can more accurately distinguish between biomes, which is currently limited by the coarse spatial resolution of TROPOMI.

The workflow employed to generate this dataset involved the gridding of L2B TROPOSIF data and the extraction of auxiliary bands. Despite the availability of a gridded L3 TROPOSIF product, it should be noted that the data does include the auxiliary bands required for this type of study, such as reflectance, SZA and VZA. The L3 and L2B products are also not available in GEE, which consequently adds an additional step to the processing chain to create such a vast dataset. In the context of GEE, the processing of MODIS data proved to be a straightforward and efficient process, largely due to the efficient computing capabilities of the system. The download of such time series data necessitated an additional processing step prior to its combination into a single coherent netCDF file. The methodology of normalization is simple and requires only the input of SIF, reflectance bands and PAR. However, the integration of the methodology into GEE, as well as the export options from GEE, would have improved the entire workflow dramatically.

4.2. Added value of a satellite-based time series of ΦF for drought monitoring

The nationwide analysis revealed that ΦF can track changes in SSWSa with a lag of two days in both agricultural and forested areas, with only localized deviations observed in the forested regions of drought-prone eastern Germany, while agricultural areas followed the same pattern. The lagged responses observed for ΦF and LST exceeded the surrogate-based Monte-Carlo confidence envelopes, whereas most other variables remained within the envelopes, supporting the robustness of these findings under autocorrelated time-series conditions. Although the average fraction of valid pixels on individual growing-season days was limited, a sensitivity analysis using rolling-average windows showed that increasing effective data availability substantially smoothed the cross-correlation curves without materially changing the dominant lag, indicating that missingness primarily affects uncertainty rather than the central timing result.The similar responses observed for both land cover classes are likely related to mixed-pixel effects, which are unavoidable at the 0.05° resolution of TROPOMI in Germany when combined with a discrete land cover dataset such as CLC. This interpretation is supported by the quantified subpixel composition of the masks: pixels assigned to forest and agriculture had median target-class fractions of only about 0.58 and 0.59, respectively, showing that both subsets represent mixed landscape mosaics rather than compositionally pure vegetation classes. Our results support previous evidence that ΦF decreases in response to drought stress within a few days, as shown at both leaf and canopy levels by De Cannière et al. (2022) and Damm et al. (2018) and at 0.25° resolution by Tang et al. (2026). The observed inverse relationship with LST further strengthens these results, indicating that the detected patterns indeed reflect physiological responses to drought stress. LST, although not part of the calculation of ΦF, was expected to be reacting sensitive to changes in SSWS anomaly as it has been used as a proxy for evapotranspiration and vegetation water stress for decades (Karnieli et al., 2010; Cunha et al., 2015). A multitude of vegetation health and drought indices have been developed that rely on a combination of LST and VIs such as the NDVI (Sandholt et al., 2002; Przeździecki et al., 2023; Carlson et al., 1990; Mu et al., 2013). The VIs component in these health and drought indices reflect the amount of vegetation that is present at a given location and complements the temperature information which by itself can vary in space and time due to land surface characteristics in vegetation, soil and topography (Sandholt et al., 2002; Le Page and Zribi, 2019).

According to plant physiological principles, and as stated by Berger et al. (2022) and Damm et al. (2018), ΦF should be the first remote sensing parameter to respond to insufficient water supply due to its direct link to photosynthesis. In our study, however, neither a faster ΦF response relative to LST nor the double SIF response (initial increase followed by a decrease) as reported by Damm et al. (2018) could be confirmed. This discrepancy is likely related to the coarse spatial resolution of TROPOSIF data and the temporal and spatial averaging, which tend to smooth short-term dynamics. Nevertheless, the decline in ΦF we observed is consistent with both 16-day and monthly satellite studies (Sun et al., 2015; Song et al., 2018) and a study based on high-frequency proximal data (De Cannière et al., 2022). It also agrees with the recent findings by Tang et al. (2026) who combine high-frequency observations with coarse 0.25° spatial resolution data. Our results therefore help to bridge the gap between plant physiological theory,field-scale experiments and coarse-resolution satellite observations.

Besides ΦF and LST, no other investigated remote sensing parameter was significantly associated with short-term changes in water availability within the analyzed 0–7 day lag window. Vegetation indices (NIRv, NDVI, NIRvP) and top-of-canopy SIF showed low cross-correlation coefficients and high variability, which is consistent with their strong dependence on vegetation phenology (e.g., leaf chlorophyll content and leaf area index) rather than short-term stress responses of plants. In particular, NIRvP, as a proxy for the structural component of SIF (Dechant et al., 2022), was not expected to respond to drought over short timescales. The resulting separation of SIF into a stress-responsive biochemical component (ΦF) and a structural component represented by vegetation indices agrees with De Cannière et al. (2022), who observed changes in ΦF while VIs remained insensitive within days. Finally, the limited suitability of top-of-canopy SIF alone to detect short-term drought effects demonstrated in this study highlights the importance of normalizing SIF to isolate the physiological information of SIF as measured by a remote sensing sensor. This finding is in line with Song et al. (2018) and Liu et al. (2021), who both reported improved drought detection using SIF yield compared to VIs or top-of-canopy SIF. Together, these results confirm that only the physiological component of SIF (ΦF), rather than the structural component represented by VIs or top-of-canopy SIF alone, provides a reliable short-term indicator of drought stress.

Current drought monitors largely rely on VIs and/or fAPAR to estimate the vegetation response component (Svoboda et al., 2002; Sepulcre-Canto et al., 2012; Trnka et al., 2020). Including information about ΦF in these monitoring schemes could improve the accuracy and timeliness of vegetation response to drought stress. In addition to fluorescence-based metrics, reflectance-based proxies of light-use efficiency such as the photochemical reflectance index (PRI) have been proposed as complementary indicators of rapid photosynthetic down-regulation under stress (Gamon et al., 1997). Although PRI has been derived from MODIS using band substitutions, implementing and validating a consistent PRI formulation at daily resolution is beyond the scope of this study and remains a promising direction for future work, particularly because PRI has been reported to be sensitive to crop type and may therefore be difficult to interpret reliably at the 0.05° pixel scale in heterogeneous landscapes (Vanikiotis et al., 2021; Zhu et al., 2024). Recent studies have combined SIF with temperature-based metrics to develop new drought indicators, such as the Temperature

Fluorescence Dryness Index (TFDI) using SIF and LST (Zhang et al., 2021b), and the SIF Health Index (SHI) and Drought Fluorescence Monitoring Index (DFMI), which pair SIF with the Temperature Condition Index (TCI) (Liu et al., 2021). The latter shows potential in early detection of soil moisture changes and could be adapted with our findings to include ΦF instead of SIF at daily temporal resolution. Additionally, the daily ΦF information could help to improve the temporal resolution of drought monitors while maintaining the same spatial resolution of 0.05°. This represents a clear advantage over global fAPAR products, which on one hand only account for the absorbed PAR radiation that potentially can be used for photosynthesis, and on the other hand have a minimal temporal resolution of 8-days. Furthermore, the dynamic nature of SIF and ΦF also makes the signal not reliant on anomaly calculations as it is directly linked to the current physiological state of vegetation. This is a major advantage for monitoring drought of agricultural areas that have changing crop rotation throughout the season, which can introduce large uncertainties in anomaly calculation.

The presented analysis serves as a first step in showing the potential of a satellite-based ΦF time series to be integrated into existing drought monitoring systems. The current analysis was based on data covering the whole of Germany and thus cannot be used for drought stress monitoring of small-scale regions. However, our study clearly shows the importance of normalizing SIF for the influence of canopy structure and illumination conditions.

4.3. Limits of the presented approach and future applications

The main limiting factor of this approach is the spatial resolution (5.5 × 3.5 km), which restricted the analysis to large, heterogeneous biomes. This inevitably leads to mixed pixels, which hide information that could further improve our understanding of the behaviour of ΦF under drought stress conditions in different biomes. Additionally, while ΦF represents the physiological state of vegetation, it can not be differentiated what kind of stress is being captured with this approach. The soil-moisture reference was based on a single layer at 0.17 m depth and should therefore be interpreted as a standardized comparison depth rather than as the exact effective root-zone depth of all vegetation types. However, the sensitivity of ΦF to multiple forms of vegetation stress can also be seen as an advantage, as it broadens its applicability for detecting different types of stress across a wide range of environmental conditions.

Nevertheless, the presented approach of using SSWSa as a drought indicator, together with its agreement with CDI-derived watch and warning periods, provides confidence that the patterns observed in this analysis are linked to drought stress. Multiple studies have explored the possibility of improving the spatial resolution of satellite SIF products using physical based approaches and machine learning (Turner et al., 2020; Gensheimer et al., 2022). While the first results seem to be promising, no operational product that can be used to create a dataset as used in this study has been made available. The spatial downscaling approaches also lack validation, which could be performed once FLEX becomes operational. This would enable not only the validation of SIF and ΦF but also comparisons with eddy-covariance tower–based GPP measurements.

The fact that we cannot directly validate our new ΦF product is also a factor that needs to be considered when interpreting the results of this study. Additionally, the used TROPOMI reflectance bands were not atmospherically corrected, which adds another layer of uncertainty to the uncertainty budget of our new ΦF product. While the L2B TROPOSIF product provides a quality band and a pixel wise uncertainty for the retrieved SIF, the BESS PAR data does not provide this information (Ryu et al., 2018; Guanter et al., 2021). Propagating uncertainties would further improve the robustness of the generated ΦF time series and increase its credibility. Future work could evaluate whether improved TROPOMI SIF retrievals based on machine-learning approaches reduce uncertainty in the derived ΦF signal such as the ANNSIF dataset by Li et al. (2025).

The workflow can be adapted to other regions using cloud computing. However, the lack of gridded TROPOSIF L2B data with corresponding reflectance bands on platforms like GEE complicates the entire procedure of calculating ΦF. Transferring the presented approach to another region, which is less influenced by clouds and more prone to drought stress (e.g. southern Europe) could further help to explore the full potential of ΦF for the early detection of drought stress. This would also enhance our understanding of the climatic conditions under which the findings of this study remain valid. However, applying this method to other regions of the world could be limited by factors such as phase angle effects and cloud contamination (Köhler et al., 2018a).

5. Conclusion

This study demonstrates the importance of normalizing SIF to better reflect the physiological state of vegetation. The connection between agricultural drought stress and ΦF at satellite scale shows that even at coarse resolution a downscaling from canopy to leaf level combined with a normalization of illumination effects is viable to gain an insight into the physiological state of vegetation. The generated daily ΦF time series over Germany enabled the detection of short-term vegetation dynamics and provided insights into physiological stress reactions, which are often masked in traditional remote sensing proxies (e.g., VIs).

The introduced workflow is readily transferable to other regions worldwide, enabling future studies focussed on vegetation stress detection across diverse large-scale biomes. While the revisit frequency of 27-days of the upcoming FLEX satellite mission (ESA, 2025) may not support continuous monitoring, FLEX will play a critical role in validating ΦF products derived from coarser-resolution satellite data such as TROPOMI and advancing retrieval and normalization methods. Finally, the integration of ΦF into existing drought monitoring frameworks, such as the Combined Drought Indicator (CDI), should be further explored. Given its daily temporal resolution and ability to directly capture physiological changes, ΦF holds strong potential to complement or improve current approaches based on vegetation indices and/or fAPAR. This is especially relevant for capturing rapid drought responses in both agricultural areas and forests, where early detection is critical for adapted resource management and the development of mitigation strategies.

CRediT authorship contribution statement

David Herrera: Writing – review & editing, Writing – original draft, Visualization, Software, Methodology, Investigation, Formal analysis, Data curation, Conceptualization. **Alexandre Belleflamme:** Writing – review & editing, Methodology, Conceptualization. **Klaus Görgen:** Methodology, Conceptualization. **Uwe Rascher:** Writing – review & editing, Writing – original draft, Supervision, Resources, Methodology, Conceptualization. **Bastian Siegmann:** Writing – review & editing, Writing – original draft, Supervision, Resources, Methodology, Funding acquisition, Conceptualization.

Declaration of generative AI and AI-assisted technologies in the writing process

During the preparation of this work the author(s) used ChatGPT in order to improve language and readability. After using this tool/service, the author(s) reviewed and edited the content as needed and take(s) full responsibility for the content of the publication.

Declaration of competing interest

The authors declare that they have no known competing financial interests or personal relationships that could have appeared to influence the work reported in this paper.

Acknowledgments

The SSWS simulation data used in this study have been developed within the project ADAPTER (Adapt Terrestrial Systems; funding reference WT-0104) funded by the Impulse and Networking Fund of the Helmholtz Association of German Research Centres. We gratefully acknowledge the Earth System Modelling Project (ESM) for funding this study by providing computing time on the ESM partition of the supercomputer JUWELS at Jülich Supercomputing Centre (JSC). This work has partially been funded by the Deutsche Forschungsgemeinschaft (DFG, German Research Foundation) under Germany's Excellence Strategy – EXC 2070 – 390732324 and the Federal German Ministry for Economic Affairs and Climate Action (BMWK) within the DroughtMAP project under the grant number 50EE2233. Open Access was funded by the Deutsche Forschungsgemeinschaft (DFG, German Research Foundation) – 491111487.

Appendix A. Supplementary data

Supplementary data to this article can be found online at https://doi.org/10.1016/j.rse.2026.115456.

Data availability

The TROPOSIF L2B products were downloaded from https://s5p-troposif.noveltis.fr/data-access/, while the BESS PAR datasets involved in the calculation of the ΦF data were obtained using GEE and downloaded from https://www.environment.snu.ac.kr/bess-rad. Additional PAR data (MCD18C2 and MCD18A2), LST data (MYD21C1/MOD21C1) and BRDF corrected reflectance data (MCD43A4) from MODIS were accessed using GEE. The ΦF dataset created in this study as well as the corresponding comparison dataset of SSWS and SSWSa is available at: doi:10.26165/JUELICH-DATA/RZ0NDZ. The original dataset including SSWS is published under: doi:10.26165/JUELICH-DATA/GROHKP.

References

Abrams, M., Crippen, R., Fujisada, H., 2020. ASTER global digital elevation model (GDEM) and ASTER global water body dataset (ASTWBD). Remote Sens. 12 (7). https://doi.org/10.3390/rs12071156. Article 7.

Badgley, G., Field, C.B., Berry, J.A., 2017. Canopy near-infrared reflectance and terrestrial photosynthesis. Sci. Adv. 3 (3), e1602244. https://doi.org/10.1126/sciadv.1602244.

Balde, H., Hmimina, G., Goulas, Y., Latouche, G., Soudani, K., 2023. Synergy between TROPOMI sun-induced chlorophyll fluorescence and MODIS spectral reflectance for understanding the dynamics of gross primary productivity at integrated carbon observatory system (ICOS) ecosystem flux sites. Biogeosciences 20 (7), 1473–1490. https://doi.org/10.5194/bg-20-1473-2023.

Belleflamme, A., Goergen, K., Wagner, N., Kollet, S., Bathiany, S., El Zohbi, J., Rechid, D., Vanderborght, J., Vereecken, H., 2023. Hydrological forecasting at impact scale: the integrated ParFlow hydrological model at 0.6 km for climate resilient water resource management over Germany. Front. Water 5. https://doi.org/10.3389/frwa.2023.1183642.

Belleflamme, A., Hammoudeh, S., Görgen, K., Kollet, S., 2024. Experimental FZJ ParFlow DE06 hydrologic forecasts [dataset]. Jülich DATA. https://doi.org/10.26165/JUELICH-DATA/GROHKP.

Berger, K., Machwitz, M., Kycko, M., Kefauver, S.C., Van Wittenberghe, S., Gerhards, M., Verrelst, J., Atzberger, C., van der Tol, C., Damm, A., Rascher, U., Herrmann, I., Paz, V.S., Fahrner, S., Pieruschka, R., Prikaziuk, E., Buchaillot, Ma.L., Halabuk, A., Celesti, M., Schlerf, M., 2022. Multi-sensor spectral synergies for crop stress detection and monitoring in the optical domain: a review. Remote Sens. Environ. 280, 113198. https://doi.org/10.1016/j.rse.2022.113198.

Bernhardt, J.J., Stupak, N., Neuenfeldt, S., Potts, F., 2026. Status quo der Bewässerung in Deutschland.

Bevacqua, E., Rakovec, O., Schumacher, D.L., Kumar, R., Thober, S., Samaniego, L., Seneviratne, S.I., Zscheischler, J., 2024. Direct and lagged climate change effects intensified the 2022 European drought. Nat. Geosci. 17 (11), 1100–1107. https://doi.org/10.1038/s41561-024-01559-2.

Boergens, E., Güntner, A., Dobslaw, H., Dahle, C., 2020. Quantifying the Central European droughts in 2018 and 2019 with GRACE follow-on. Geophys. Res. Lett. 47 (14), e2020GL087285. https://doi.org/10.1029/2020GL087285.

Bundesministerium für Ernährung und Landwirtschaft, 2025. Landwirtschaftlicher Bodenmarkt in Deutschland [WWW Document]. BMEL. URL. https://www.bmel.de/DE/themen/landwirtschaft/flaechennutzung-und-bodenmarkt/bodenmarkt-deutschland-landwirtschaft.html (accessed 7.11.25).

Cammalleri, C., Arias-Muñoz, C., Barbosa, P., de Jager, A., Magni, D., Masante, D., Mazzeschi, M., McCormick, N., Naumann, G., Spinoni, J., Vogt, J., 2021. A revision of the combined drought indicator (CDI) used in the European drought observatory (EDO). Nat. Hazards Earth Syst. Sci. 21 (2), 481–495. https://doi.org/10.5194/nhess-21-481-2021.

Carlson, T.N., Perry, E.M., Schmugge, T.J., 1990. Remote estimation of soil moisture availability and fractional vegetation cover for agricultural fields. Agric. For. Meteorol. 52 (1), 45–69. https://doi.org/10.1016/0168-1923(90)90100-K.

Carrão, H., Naumann, G., Barbosa, P., 2016. Mapping global patterns of drought risk: an empirical framework based on sub-national estimates of hazard, exposure and vulnerability. Glob. Environ. Chang. 39, 108–124. https://doi.org/10.1016/j.gloenvcha.2016.04.012.

CORINE Land Cover 2018 (vector), Europe, 6-yearly—Version 2020_20u1, May 2020. In: EEA Geospatial Data Catalogue, 2026. Retrieved September 20, 2025, from. https://sdi.eea.europa.eu/catalogue/copernicus/api/records/71c95a07-e296-44fc-b22b-415f42acfdf0.

Cunha, A.P.M., Alvalá, R.C., Nobre, C.A., Carvalho, M.A., 2015. Monitoring vegetative drought dynamics in the Brazilian semiarid region. Agric. For. Meteorol. 214–215, 494–505. https://doi.org/10.1016/j.agrformet.2015.09.010.

Dai, Y., Zeng, X., Dickinson, R.E., Baker, I., Bonan, G.B., Bosilovich, M.G., Denning, A.S., Dirmeyer, P.A., Houser, P.R., Niu, G., Oleson, K.W., Schlosser, C.A., Yang, Z.-L., 2003. The common land model. Bull. Am. Meteorol. Soc. 84 (8), 1013–1024. https://doi.org/10.1175/BAMS-84-8-1013.

Damm, A., Paul-Limoges, E., Haghighi, E., Simmer, C., Morsdorf, F., Schneider, F.D., van der Tol, C., Migliavacca, M., Rascher, U., 2018. Remote sensing of plant-water relations: an overview and future perspectives. J. Plant Physiol. 227, 3–19. https://doi.org/10.1016/j.jplph.2018.04.012.

De Cannière, S., Vereecken, H., Defourny, P., Jonard, F., 2022. Remote sensing of instantaneous drought stress at canopy level using Sun-induced chlorophyll fluorescence and canopy reflectance. Remote Sens. 14 (11). https://doi.org/10.3390/rs14112642. Article 11.

De Cannière, S., Baur, M.J., Chaparro, D., Jagdhuber, T., Jonard, F., 2024. Water availability and atmospheric dryness controls on spaceborne sun-induced chlorophyll fluorescence yield. Remote Sens. Environ. 301, 113922. https://doi.org/10.1016/j.rse.2023.113922.

Dechant, B., Ryu, Y., Badgley, G., Zeng, Y., Berry, J.A., Zhang, Y., Goulas, Y., Li, Z., Zhang, Q., Kang, M., Li, J., Moya, I., 2020. Canopy structure explains the relationship between photosynthesis and sun-induced chlorophyll fluorescence in crops. Remote Sens. Environ. 241, 111733. https://doi.org/10.1016/j.rse.2020.111733.

Dechant, B., Ryu, Y., Badgley, G., Köhler, P., Rascher, U., Migliavacca, M., Zhang, Y., Tagliabue, G., Guan, K., Rossini, M., Goulas, Y., Zeng, Y., Frankenberg, C., Berry, J. A., 2022. NIRVP: A robust structural proxy for sun-induced chlorophyll fluorescence and photosynthesis across scales. Remote Sens. Environ. 268, 112763. https://doi.org/10.1016/j.rse.2021.112763.

Doughty, R., Köhler, P., Frankenberg, C., Magney, T.S., Xiao, X., Qin, Y., Wu, X., Moore, B., 2019. TROPOMI reveals dry-season increase of solar-induced chlorophyll fluorescence in the amazon forest. Proc. Natl. Acad. Sci. 116 (44), 22393–22398. https://doi.org/10.1073/pnas.1908157116.

Drusch, M., Moreno, J., Del Bello, U., Franco, R., Goulas, Y., Huth, A., Kraft, S., Middleton, E.M., Miglietta, F., Mohammed, G., Nedbal, L., Rascher, U., Schüttemeyer, D., Verhoef, W., 2017. The FLuorescence EXplorer Mission concept—ESA'S earth Explorer 8. IEEE Trans. Geosci. Remote Sens. 55 (3), 1273–1284. https://doi.org/10.1109/TGRS.2016.2621820.

Du, S., Liu, X., Chen, J., Duan, W., Liu, L., 2023. Addressing validation challenges for TROPOMI solar-induced chlorophyll fluorescence products using tower-based measurements and an NIRv-scaled approach. Remote Sens. Environ. 290, 113547. https://doi.org/10.1016/j.rse.2023.113547.

Duscher, K., Günther, A., Richts, A., Clos, P., Philipp, U., Struckmeier, W., 2015. The GIS layers of the "international hydrogeological map of Europe 1: 1,500,000" in a vector format. Hydrogeol. J. 23 (8), 1867–1875. https://doi.org/10.1007/s10040-015-1296-4.

European Commission, Joint Research Centre (JRC), 2022. EDO Combined Drought Indicator (CDI) (version 4.0.0). European Commission, Joint Research Centre (JRC). https://doi.org/10.2905/afa8a5ee-5473-439a-b062-ffdaedc38b2d. PID. http://data.europa.eu/89h/afa8a5ee-5473-439a-b062-ffdaedc38b2d.

European Space Agency, 2025. FLEX [WWW Document]. URL. https://www.esa.int/Applications/Observing_the_Earth/FutureEO/FLEX (accessed 7.11.25).

Fensholt, R., Sandholt, I., Rasmussen, M.S., 2004. Evaluation of MODIS LAI, fAPAR and the relation between fAPAR and NDVI in a semi-arid environment using in situ measurements. Remote Sens. Environ. 91 (3), 490–507. https://doi.org/10.1016/j.rse.2004.04.009.

Fioravanti, G., Toreti, A., Cammalleri, C., Muñoz, C.A., Bavera, D., De Jager, A., Hrast Essenfelder, A., Di Ciollo, C., Masante, D., Magni, D., Navarro, J.A., Mazzesch, M., Maetens, W., 2025. A dataset for monitoring agricultural drought in Europe. Sci. Data 12 (1), 308. https://doi.org/10.1038/s41597-024-04199-8.

Frankenberg, C., Fisher, J.B., Worden, J., Badgley, G., Saatchi, S.S., Lee, J.-E., Toon, G.C., Butz, A., Jung, M., Kuze, A., Yokota, T., 2011. New global observations of the terrestrial carbon cycle from GOSAT: patterns of plant fluorescence with gross primary productivity. Geophys. Res. Lett. 38 (17). https://doi.org/10.1029/2011GL048738.

Frankenberg, C., O'Dell, C., Guanter, L., McDuffie, J., 2012. Remote sensing of near-infrared chlorophyll fluorescence from space in scattering atmospheres: implications

for its retrieval and interferences with atmospheric CO_2 retrievals. Atmos. Meas. Tech. 5 (8), 2081–2094. https://doi.org/10.5194/amt-5-2081-2012.
Gamon, J.A., Serrano, L., Surfus, J.S., 1997. The photochemical reflectance index: an optical indicator of photosynthetic radiation use efficiency across species, functional types, and nutrient levels. Oecologia 112, 492–501. https://doi.org/10.1007/s004420050337.
Geng, G., Yang, R., Liu, L., 2022. Downscaled solar-induced chlorophyll fluorescence has great potential for monitoring the response of vegetation to drought in the yellow river basin, China: insights from an extreme event. Ecol. Indic. 138, 108801. https://doi.org/10.1016/j.ecolind.2022.108801.
Gensheimer, J., Turner, A.J., Köhler, P., Frankenberg, C., Chen, J., 2022. A convolutional neural network for spatial downscaling of satellite-based solar-induced chlorophyll fluorescence (SIFnet). Biogeosciences 19 (6), 1777–1793. https://doi.org/10.5194/bg-19-1777-2022.
German Environment Agency, 2024. 2023 Monitoring Report on the German Strategy for Adaptation to Climate Change. https://doi.org/10.60810/openumwelt-2309.
Gorelick, N., Hancher, M., Dixon, M., Ilyushchenko, S., Thau, D., Moore, R., 2017. Google earth engine: planetary-scale geospatial analysis for everyone. Remote Sens. Environ. 202, 18–27. https://doi.org/10.1016/j.rse.2017.06.031.
Guanter, L., Frankenberg, C., Dudhia, A., Lewis, P.E., Gómez-Dans, J., Kuze, A., Suto, H., Grainger, R.G., 2012. Retrieval and global assessment of terrestrial chlorophyll fluorescence from GOSAT space measurements. Remote Sens. Environ. 121, 236–251. https://doi.org/10.1016/j.rse.2012.02.006.
Guanter, L., Zhang, Y., Jung, M., Joiner, J., Voigt, M., Berry, J.A., Frankenberg, C., Huete, A.R., Zarco-Tejada, P., Lee, J.-E., Moran, M.S., Ponce-Campos, G., Beer, C., Camps-Valls, G., Buchmann, N., Gianelle, D., Klumpp, K., Cescatti, A., Baker, J.M., Griffis, T.J., 2014. Global and time-resolved monitoring of crop photosynthesis with chlorophyll fluorescence. Proc. Natl. Acad. Sci. 111 (14). https://doi.org/10.1073/pnas.1320008111.
Guanter, L., Bacour, C., Schneider, A., Aben, I., van Kempen, T.A., Maignan, F., Retscher, C., Köhler, P., Frankenberg, C., Joiner, J., Zhang, Y., 2021. The TROPOSIF global sun-induced fluorescence dataset from the sentinel-5P TROPOMI mission. Earth Syst. Sci. Data 13 (11), 5423–5440. https://doi.org/10.5194/essd-13-5423-2021.
Hapke, B., 2012. Theory of Reflectance and Emittance Spectroscopy. Cambridge University Press.
Hari, V., Rakovec, O., Markonis, Y., Hanel, M., Kumar, R., 2020. Increased future occurrences of the exceptional 2018–2019 central European drought under global warming. Sci. Rep. 10 (1), 12207. https://doi.org/10.1038/s41598-020-68872-9.
Hengl, T., de Jesus, J.M., Heuvelink, G.B.M., Gonzalez, M.R., Kilibarda, M., Blagotić, A., Shangguan, W., Wright, M.N., Geng, X., Bauer-Marschallinger, B., Guevara, M.A., Vargas, R., MacMillan, R.A., Batjes, N.H., Leenaars, J.G.B., Ribeiro, E., Wheeler, I., Mantel, S., Kempen, B., 2017. SoilGrids250m: global gridded soil information based on machine learning. PLoS One 12 (2), e0169748. https://doi.org/10.1371/journal.pone.0169748.
Hua, L., Wang, H., Sui, H., Wardlow, B., Hayes, M.J., Wang, J., 2019. Mapping the spatial-temporal dynamics of vegetation response lag to drought in a semi-arid region. Remote Sens. 11 (16). https://doi.org/10.3390/rs11161873. Article 16.
Hulley, G., Hook, S., 2025. MODIS/Aqua Land Surface Temperature/3-Band Emissivity Daily l3 Global 0.05Deg CMG v061 [Dataset]. NASA EOSDIS Land Processes Distributed Active Archive Center. https://doi.org/10.5067/MODIS/MYD21C1.061.
Jiang, C., Guan, K., Wu, G., Peng, B., Wang, S., 2021. A daily, 250m and real-time gross primary productivity product (2000–present) covering the contiguous United States. Earth Syst. Sci. Data 13 (2), 281–298. https://doi.org/10.5194/essd-13-281-2021.
Joiner, J., Yoshida, Y., Vasilkov, A.P., Yoshida, Y., Corp, L.A., Middleton, E.M., 2011. First observations of global and seasonal terrestrial chlorophyll fluorescence from space. Biogeosciences 8 (3), 637–651. https://doi.org/10.5194/bg-8-637-2011.
Karnieli, A., Agam, N., Pinker, R.T., Anderson, M., Imhoff, M.L., Gutman, G.G., Panov, N., Goldberg, A., 2010. Use of NDVI and land surface temperature for drought assessment: merits and limitations. J. Clim. 23 (3), 618–633. https://doi.org/10.1175/2009JCLI2900.1.
Köhler, P., Frankenberg, C., Magney, T.S., Guanter, L., Joiner, J., Landgraf, J., 2018a. Global retrievals of solar-induced chlorophyll fluorescence with TROPOMI: first results and intersensor comparison to OCO-2. Geophys. Res. Lett. 45 (19), 10456–10463. https://doi.org/10.1029/2018GL079031.
Köhler, P., Guanter, L., Kobayashi, H., Walther, S., Yang, W., 2018b. Assessing the potential of sun-induced fluorescence and the canopy scattering coefficient to track large-scale vegetation dynamics in amazon forests. Remote Sens. Environ. 204, 769–785. https://doi.org/10.1016/j.rse.2017.09.025.
Kuffour, B.N.O., Engdahl, N.B., Woodward, C.S., Condon, L.E., Kollet, S., Maxwell, R.M., 2020. Simulating coupled surface–subsurface flows with ParFlow v3.5.0: capabilities, applications, and ongoing development of an open-source, massively parallel, integrated hydrologic model. Geosci. Model Dev. 13 (3), 1373–1397. https://doi.org/10.5194/gmd-13-1373-2020.
Le Page, M., Zribi, M., 2019. Analysis and predictability of drought in northwest Africa using optical and microwave satellite remote sensing products. Sci. Rep. 9 (1), 1466. https://doi.org/10.1038/s41598-018-37911-x.
Li, W., Pacheco-Labrador, J., Migliavacca, M., Miralles, D., Hoek van Dijke, A., Reichstein, M., Forkel, M., Zhang, W., Frankenberg, C., Panwar, A., Zhang, Q., Weber, U., Gentine, P., Orth, R., 2023a. Widespread and complex drought effects on vegetation physiology inferred from space. Nat. Commun. 14, 4640. https://doi.org/10.1038/s41467-023-40226-9.
Li, M., Sun, H., Zhao, R., 2023b. A review of root zone soil moisture estimation methods based on remote sensing. Remote Sens. 15 (22). https://doi.org/10.3390/rs15225361. Article 22.
Li, D., Chen, J.M., Duveiller, G., Frankenberg, C., Köhler, P., Yu, K., 2025. A more precise retrieval of sun-induced chlorophyll fluorescence from satellite data using artificial neural networks. Remote Sens. Environ. 330, 114987. https://doi.org/10.1016/j.rse.2025.114987.
Liu, Y., Dang, C., Yue, H., Lyu, C., Dang, X., 2021. Enhanced drought detection and monitoring using sun-induced chlorophyll fluorescence over Hulun Buir Grassland, China. Sci. Total Environ. 770, 145271. https://doi.org/10.1016/j.scitotenv.2021.145271.
Liu, X., Liu, L., Bacour, C., Guanter, L., Chen, J., Ma, Y., Chen, R., Du, S., 2023a. A simple approach to enhance the TROPOMI solar-induced chlorophyll fluorescence product by combining with canopy reflected radiation at near-infrared band. Remote Sens. Environ. 284, 113341. https://doi.org/10.1016/j.rse.2022.113341.
Liu, Y., Yu, X., Dang, C., Yue, H., Wang, X., Niu, H., Zu, P., Cao, M., 2023b. A dryness index TSWDI based on land surface temperature, sun-induced chlorophyll fluorescence, and water balance. ISPRS J. Photogramm. Remote Sens. 202, 581–598. https://doi.org/10.1016/j.isprsjprs.2023.07.005.
Mu, Q., Zhao, M., Kimball, J.S., McDowell, N.G., Running, S.W., 2013. A remotely sensed global terrestrial drought severity index. Bull. Am. Meteorol. Soc. 94 (1), 83–98. https://doi.org/10.1175/BAMS-D-11-00213.1.
Owens, R., Hewson, T., 2018. ECMWF forecast user guide. ECMWF. https://doi.org/10.21957/M1CS7H.
Pickering, M., Cescatti, A., Duveiller, G., 2022. Sun-induced fluorescence as a proxy for primary productivity across vegetation types and climates. Biogeosciences 19 (20), 4833–4864. https://doi.org/10.5194/bg-19-4833-2022.
Przeździecki, K., Zawadzki, J.J., Urbaniak, M., Ziemblińska, K., Miatkowski, Z., 2023. Using temporal variability of land surface temperature and normalized vegetation index to estimate soil moisture condition on forest areas by means of remote sensing. Ecol. Indic. 148, 110088. https://doi.org/10.1016/j.ecolind.2023.110088.
Quirós, E., Fragoso-Campón, L., 2024. Spatial analysis of remote sensing and meteorological indices in a drought event in southwestern Spain. Theor. Appl. Climatol. 155 (5), 3757–3770. https://doi.org/10.1007/s00704-024-04846-5.
Rakovec, O., Samaniego, L., Hari, V., Markonis, Y., Moravec, V., Thober, S., Hanel, M., Kumar, R., 2022. The 2018–2020 multi-year drought sets a new benchmark in Europe. Earth's Future 10 (3), e2021EF002394. https://doi.org/10.1029/2021EF002394.
Roy, Samapriya, 2025. samapriya/geeup: geeup: Simple CLI for Earth Engine Uploads (2.0.0). Zenodo. https://doi.org/10.5281/zenodo.18073520.
Ryu, Y., Jiang, C., Kobayashi, H., Detto, M., 2018. MODIS-derived global land products of shortwave radiation and diffuse and total photosynthetically active radiation at 5 km resolution from 2000. Remote Sens. Environ. 204, 812–825. https://doi.org/10.1016/j.rse.2017.09.021.
Sandholt, I., Rasmussen, K., Andersen, J., 2002. A simple interpretation of the surface temperature/vegetation index space for assessment of surface moisture status. Remote Sens. Environ. 79 (2), 213–224. https://doi.org/10.1016/S0034-4257(01)00274-7.
Schaaf, C., Wang, Z., 2021. MODIS/Terra+aqua BRDF/Albedo Nadir BRDF Adjusted Ref Daily l3 Global - 500m v061 [Data Set]. NASA Land Processes Distributed Active Archive Center. https://doi.org/10.5067/MODIS/MCD43A4.061 Date Accessed: 2026-01-20.
Schaap, M.G., Leij, F.J., van Genuchten, M.Th., 2001. Rosetta: a computer program for estimating soil hydraulic parameters with hierarchical pedotransfer functions. J. Hydrol. 251 (3), 163–176. https://doi.org/10.1016/S0022-1694(01)00466-8.
Schulzweida, U., 2023. CDO User Guide. https://zenodo.org/records/10020800.
Senf, C., Seidl, R., 2021. Persistent impacts of the 2018 drought on forest disturbance regimes in Europe. Biogeosciences 18 (18), 5223–5230. https://doi.org/10.5194/bg-18-5223-2021.
Sepulcre-Canto, G., Horion, S., Singleton, A., Carrao, H., Vogt, J., 2012. Development of a combined drought indicator to detect agricultural drought in Europe. Nat. Hazards Earth Syst. Sci. 12 (11), 3519–3531. https://doi.org/10.5194/nhess-12-3519-2012.
Song, L., Guanter, L., Guan, K., You, L., Huete, A., Ju, W., Zhang, Y., 2018. Satellite sun-induced chlorophyll fluorescence detects early response of winter wheat to heat stress in the Indian indo-Gangetic plains. Glob. Chang. Biol. 24 (9), 4023–4037. https://doi.org/10.1111/gcb.14302.
Sun, Y., Fu, R., Dickinson, R., Joiner, J., Frankenberg, C., Gu, L., Xia, Y., Fernando, N., 2015. Drought onset mechanisms revealed by satellite solar-induced chlorophyll fluorescence: insights from two contrasting extreme events. J. Geophys. Res. Biogeosci. 120 (11), 2427–2440. https://doi.org/10.1002/2015JG003150.
Svoboda, M., LeComte, D., Hayes, M., Heim, R., Gleason, K., Angel, J., Rippey, B., Tinker, R., Palecki, M., Stooksbury, D., Miskus, D., Stephens, S., 2002. The drought monitor. Bull. Am. Meteorol. Soc. 83 (8), 1181–1190. https://doi.org/10.1175/1520-0477-83.8.1181.
Tang, Z., Miralles, D.G., Guo, Z., Maes, W.H., 2026. Fast response of satellite fluorescence-derived plant physiology to drought stress. Nat. Commun. 17, 2886. https://doi.org/10.1038/s41467-026-70076-0.
Trnka, M., Hlavinka, P., Možný, M., Semerádová, D., Štěpánek, P., Balek, J., Bartošová, L., Zahradníček, P., Bláhová, M., Skalák, P., Farda, A., Hayes, M., Svoboda, M., Wagner, W., Eitzinger, J., Fischer, M., Žalud, Z., 2020. Czech drought monitor system for monitoring and forecasting agricultural drought and drought impacts. Int. J. Climatol. 40 (14), 5941–5958. https://doi.org/10.1002/joc.6557.
Turner, A.J., Köhler, P., Magney, T.S., Frankenberg, C., Fung, I., Cohen, R.C., 2020. A double peak in the seasonality of Californias photosynthesis as observed from space. Biogeosciences 17 (2), 405–422. https://doi.org/10.5194/bg-17-405-2020.
Vanikiotis, T., Stagakis, S., Kyparissis, A., 2021. MODIS PRI performance to track light use efficiency of a Mediterranean coniferous forest: determinants, restrictions and the role of LUE range. Agric. For. Meteorol. 307, 108518. https://doi.org/10.1016/j.agrformet.2021.108518.

Veefkind, J.P., Aben, I., McMullan, K., Förster, H., de Vries, J., Otter, G., Claas, J., Eskes, H.J., de Haan, J.F., Kleipool, Q., van Weele, M., Hasekamp, O., Hoogeveen, R., Landgraf, J., Snel, R., Tol, P., Ingmann, P., Voors, R., Kruizinga, B., Levelt, P.F., 2012. TROPOMI on the ESA sentinel-5 precursor: A GMES mission for global observations of the atmospheric composition for climate, air quality and ozone layer applications. Remote Sens. Environ. 120, 70–83. https://doi.org/10.1016/j.rse.2011.09.027.

Vitale, D., Fratini, G., Helfter, C., Hortnagl, L., Kohonen, K.-M., Mammarella, I., Nemitz, E., Nicolini, G., Rebmann, C., Sabbatini, S., Papale, D., 2024. A pre-whitening with block-bootstrap cross-correlation procedure for temporal alignment of data sampled by eddy covariance systems. Environ. Ecol. Stat. 31, 219–244. https://doi.org/10.1007/s10651-024-00615-9.

Wang, C., Guan, K., Peng, B., Chen, M., Jiang, C., Zeng, Y., Wu, G., Wang, S., Wu, J., Yang, X., Frankenberg, C., Köhler, P., Berry, J., Bernacchi, C., Zhu, K., Alden, C., Miao, G., 2020a. Satellite footprint data from OCO-2 and TROPOMI reveal significant spatio-temporal and inter-vegetation type variabilities of solar-induced fluorescence yield in the U.S. Midwest. Remote Sens. Environ. 241, 111728. https://doi.org/10.1016/j.rse.2020.111728.

Wang, D., Liang, S., Zhang, Y., Gao, X., Brown, M.G.L., Jia, A., 2020b. A new set of MODIS land products (MCD18): downward shortwave radiation and photosynthetically active radiation. Remote Sens. 12 (1). https://doi.org/10.3390/rs12010168. Article 1.

Wen, J., Tagliabue, G., Rossini, M., Fava, F.P., Panigada, C., Merbold, L., Leitner, S., Sun, Y., 2025. Detection of fast-changing intra-seasonal vegetation dynamics of drylands using solar-induced chlorophyll fluorescence (SIF). Biogeosciences 22, 2049–2067. https://doi.org/10.5194/bg-22-2049-2025.

West, H., Quinn, N., Horswell, M., 2019. Remote sensing for drought monitoring & impact assessment: progress, past challenges and future opportunities. Remote Sens. Environ. 232, 111291. https://doi.org/10.1016/j.rse.2019.111291.

Yamazaki, D., Ikeshima, D., Sosa, J., Bates, P.D., Allen, G.H., Pavelsky, T.M., 2019. MERIT hydro: a high-resolution global hydrography map based on latest topography dataset. Water Resour. Res. 55 (6), 5053–5073. https://doi.org/10.1029/2019WR024873.

Yang, P., van der Tol, C., Campbell, P.K.E., Middleton, E.M., 2020. Fluorescence correction vegetation index (FCVI): A physically based reflectance index to separate physiological and non-physiological information in far-red sun-induced chlorophyll fluorescence. Remote Sens. Environ. 240, 111676. https://doi.org/10.1016/j.rse.2020.111676.

Zeng, Y., Badgley, G., Dechant, B., Ryu, Y., Chen, M., Berry, J.A., 2019. A practical approach for estimating the escape ratio of near-infrared solar-induced chlorophyll fluorescence. Remote Sens. Environ. 232, 111209. https://doi.org/10.1016/j.rse.2019.05.028.

Zeng, Y., Hao, D., Badgley, G., Damm, A., Rascher, U., Ryu, Y., Johnson, J., Krieger, V., Wu, S., Qiu, H., Liu, Y., Berry, J.A., Chen, M., 2021. Estimating near-infrared reflectance of vegetation from hyperspectral data. Remote Sens. Environ. 267, 112723. https://doi.org/10.1016/j.rse.2021.112723.

Zeng, Y., Hao, D., Huete, A., Dechant, B., Berry, J., Chen, J.M., Joiner, J., Frankenberg, C., Bond-Lamberty, B., Ryu, Y., Xiao, J., Asrar, G.R., Chen, M., 2022. Optical vegetation indices for monitoring terrestrial ecosystems globally. Nat. Rev. Earth Environ. 3 (7). https://doi.org/10.1038/s43017-022-00298-5. Article 7.

Zhang, Z., Chen, J., Guanter, L., He, L., Zhang, Y., 2019. From canopy-leaving to total canopy far-red fluorescence emission for remote sensing of photosynthesis: first results from TROPOMI. Geophys. Res. Lett. https://doi.org/10.1029/2019GL084832.

Zhang, Z., Xu, W., Qin, Q., Long, Z., 2021a. Downscaling solar-induced chlorophyll fluorescence based on convolutional neural network method to monitor agricultural drought. IEEE Trans. Geosci. Remote Sens. 59 (2), 1012–1028. https://doi.org/10.1109/TGRS.2020.2999371.

Zhang, J., Zhang, Z., Chen, J., Chen, H., Jin, J., Han, J., Wang, X., Song, Z., Wei, G., 2021b. Estimating soil salinity with different fractional vegetation cover using remote sensing. Land Degrad. Dev. 32 (2), 597–612. https://doi.org/10.1002/ldr.3737.

Zhu, X., Li, Q., Guo, C., 2024. Evaluation of the monitoring capability of various vegetation indices and mainstream satellite band settings for grassland drought. Eco. Inform. 82, 102717. https://doi.org/10.1016/j.ecoinf.2024.102717.

Zink, M., Samaniego, L., Kumar, R., Thober, S., Mai, J., Schaefer, D., Marx, A., 2016. The German drought monitor. Environ. Res. Lett. 11 (7), 074002. https://doi.org/10.1088/1748-9326/11/7/074002.